Chapter 6

Flat Flame Study : Experimental Results and Analysis

The philosophy and the objectives detailed in Chapter 4, Section 4.1 have highlighted the need to study simple premixed laminar flat flames for their dynamic character. To perform such a study, a laminar flat flame burner described in Chapter 4 was built and experiments were conducted following the experimental data collection and the data reduction procedures described in Chapter 5. Since methane, propane, and ethane are the three major constituents of natural gas and as one of the objectives of this laminar flame dynamic study was to analyze the effects of chemical kinetics on the flame dynamics, experiments were conducted by burning three pure fuels, methane, propane and ethane. For each of these fuels, experiments were performed for four total flow rates (Q_{Total}), and five equivalence ratios (Φ). This chapter presents the results, analysis and discussion of this experimental study in groups classified on the basis of the fuel burnt.

6.1 Experimental System Characterization

The laminar flat flame burner described in Chapter 4 was designed to stabilize laminar flat flames using the concept of excess enthalpy flames. Therefore, a strong heat transfer interaction between the flame and the honeycomb, and also between the honeycomb and

Table 6.1: Temperatures measured at the top and bottom surface of the honeycomb for experiments using methane

Total Flow Q_{Total} cc/sec	Equivalence Ratio (Φ)	Top Surface Temperature Kelvin	Bottom Surface Temperature Kelvin
145	0.5	641.28	328.16
145	0.55	798.61	340.23
145	0.6	902.6	347.94
145	0.65	958.51	354.19
145	0.75	1064.21	365.52
160	0.5	733.17	332.75
160	0.55	865.79	341.67
160	0.6	958.51	345.53
160	0.65	1015.66	355.64
160	0.75	1095	358.53
180	0.5	780.37	326.95
180	0.55	893.89	332.99
180	0.6	994.8	341.43
180	0.65	1043.75	345.29
180	0.75	1134.6	351.58
200	0.5	789.51	323.8
200	0.55	913.02	326.95
200	0.6	1024.79	330.1
200	0.65	1059.32	333.24
200	0.75	1161.01	276.05

the reactant stream is expected. This is verified by the high mean temperature of the top surface of the honeycomb and a rather low mean temperature of its bottom surface recorded for all the experimental conditions, and tabulated in Table 6.1. A'Type R' and a 'Type K' thermocouple were used to measure the temperature of the top and the bottom surface of the honeycomb respectively.

The temperature of the fuel-air mixture just prior to the flame front strongly influences the chemical reaction rate, the heat release rate and hence the flame speed. Furthermore, this reactant temperature is dependent on the heat transfer interaction between the flame and

the honeycomb, thus forming a closed loop dynamic system between the burner and the flame. Therefore, the dynamics of the burner and the flame cannot be decoupled and u' cannot be corrected for the spatial distance between the plane of u' measurement and the burner exit, as was done in the earlier work by Riley [41].

6.2 Experimental Results of Methane Combustion

Experiments were conducted with bottled instrument grade methane as fuel for five equivalence ratios ranging from 0.5 to 0.75, and four flow rates ranging from 145 cc/sec to 200 cc/sec. Laminar flat flames with $\Phi < 0.5$ could not be stabilized. The upper bound on Φ was defined by the values encountered in lean-premixed land based gas turbines. The lowest flow rate studied was limited by the maximum temperature rating of the insulated microphone wires used in the velocity measurement. The temperature of the top surface of the honeycomb defined the upper bound for the maximum flow rate studied. Although, the ceramic material of the honeycomb is rated for temperatures much higher than those recorded in these experiments, the temperature limitation arose due to the poor thermal cycling life span of the ceramic material. Frequent cyclic heating and cooling of the honeycomb causes crumbling of its top surface, thus generating minute pits on it's surface. The presence of these small pits would have adversely effected the flame structure, a condition that was undesirable for the success of this experiment.

6.2.1 Parametric Interpretation of the Experimental Results

Figure 6.1 through Figure 6.8 show the magnitude and the phase of the FRF between the OH^* chemiluminescence signal and the velocity fluctuations u' for the four flow rates starting with 145 cc/sec and ascending to 200 cc/sec. All of the experimental data discussed here is in the frequency range of 20 to 380 Hz, except for the condition of $\Phi = 0.5$ and $Q_{Total} = 145$ cc/sec, where the presented data was taken for the frequency range of 20 to 210 Hz, as the coherence between the OH^* chemiluminescence and the velocity perturbations was poor

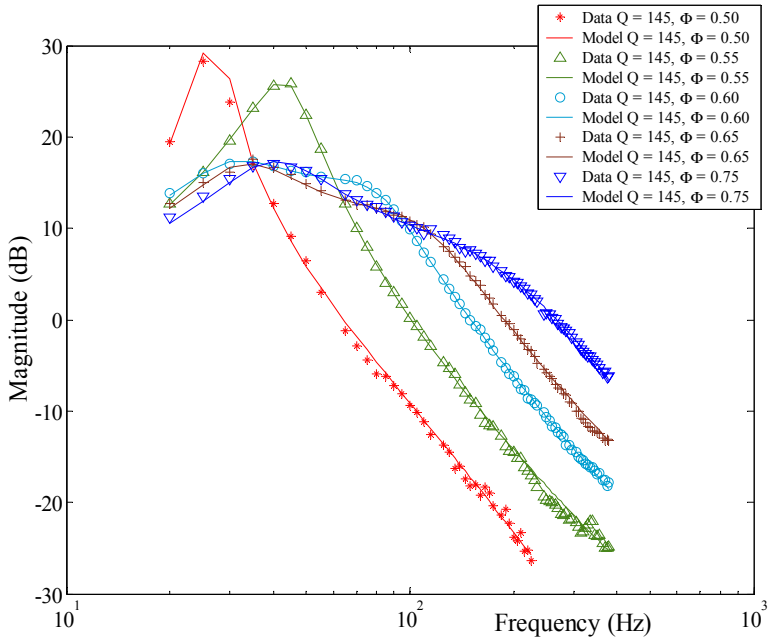

Figure 6.1: FRF (magnitude) for $Q_{Total} = 145$ cc/sec and methane-air mixture

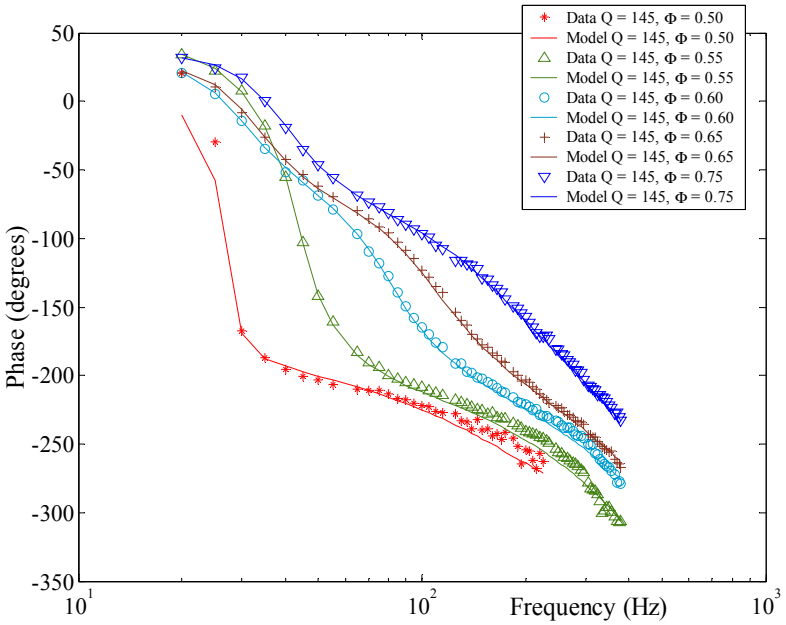

Figure 6.2: FRF (phase) for $Q_{Total} = 145$ cc/sec and methane-air mixture

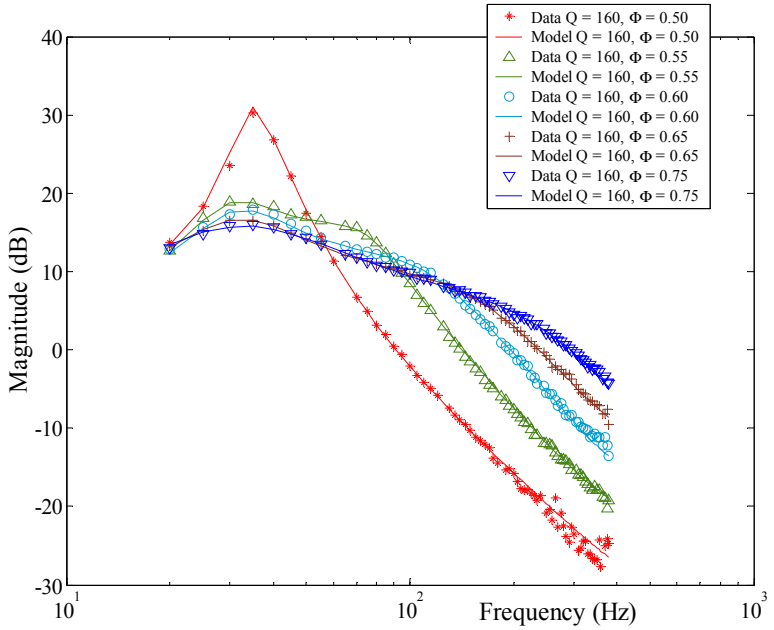

Figure 6.3: FRF (magnitude) for $Q_{Total} = 160$ cc/sec and methane-air mixture

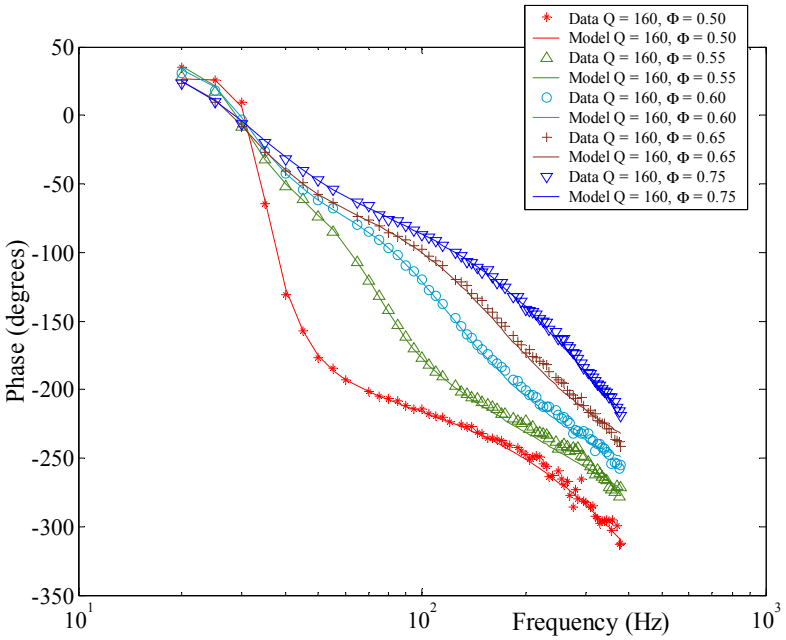

Figure 6.4: FRF (phase) for $Q_{Total} = 160$ cc/sec and methane-air mixture

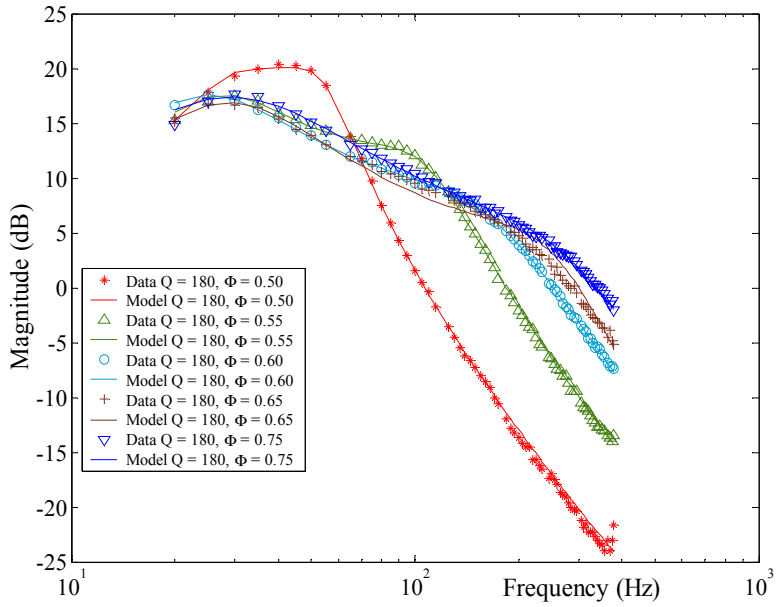

Figure 6.5: FRF (magnitude) for $Q_{Total} = 180$ cc/sec and methane-air mixture

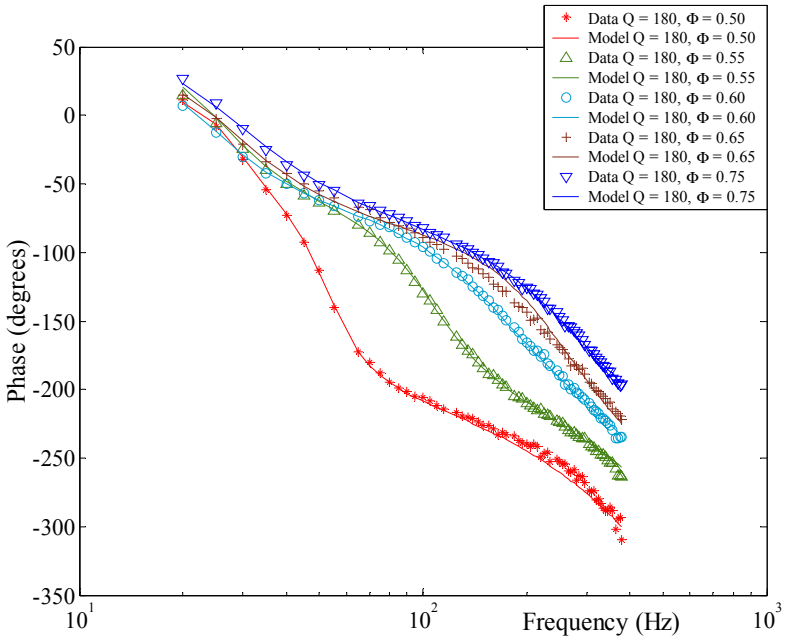

Figure 6.6: FRF (phase) for $Q_{Total} = 180$ cc/sec and methane-air mixture

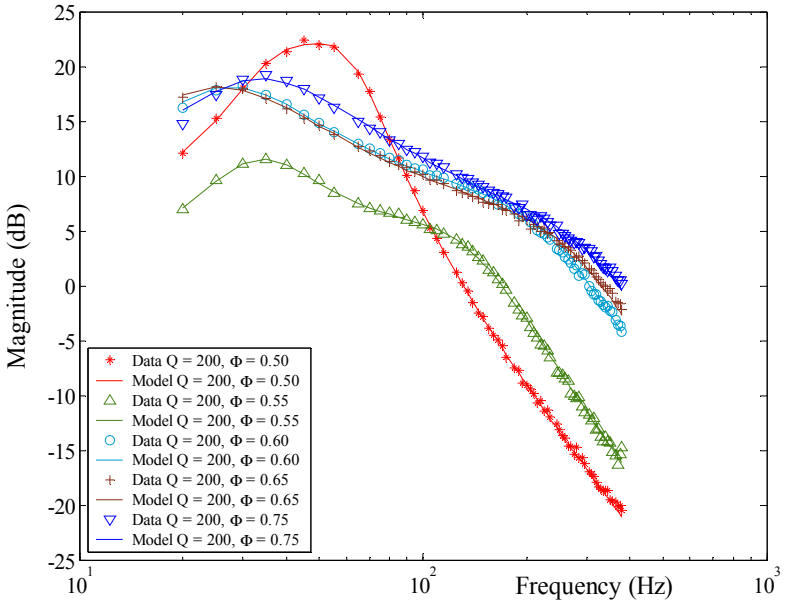

Figure 6.7: FRF (magnitude) for $Q_{Total} = 200$ cc/sec and methane-air mixture

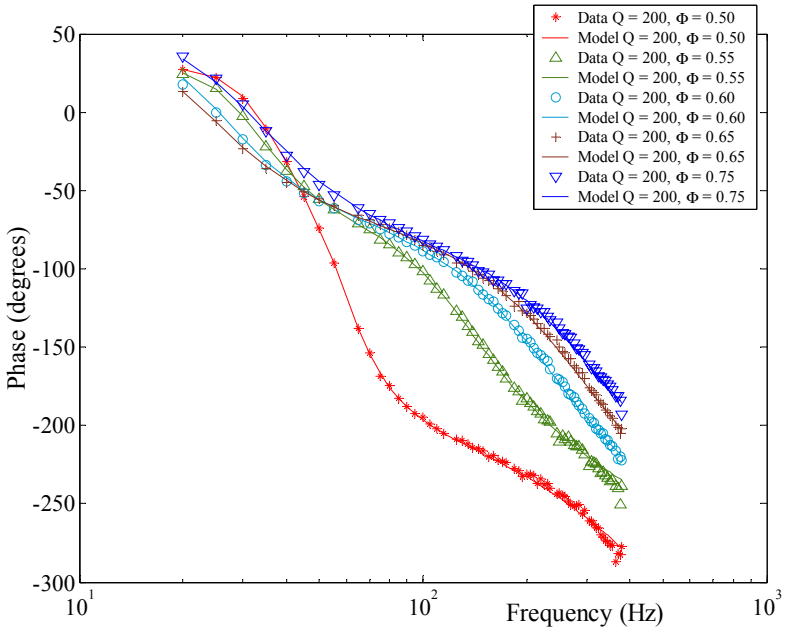

Figure 6.8: FRF (phase) for $Q_{Total} = 200$ cc/sec and methane-air mixture

beyond 210 Hz.

Figures 6.1, 6.3, 6.5, and 6.7 detail the magnitude of the FRF. These figures show that for most of the test conditions studied, there are two clearly visible damped resonant peaks, indicating that the FRF is fourth order in nature. The two resonances are clearly seen at higher Φ, while at lower Φ they are at frequencies very close to one another making it difficult to visualize and identify their presence in the plots. But the models generated to match the experimental data that are discussed later in Section 6.2.3, clearly show their presence in all of the experimental conditions studied. For the purpose of further analysis, of the two resonances, the one that occurs at a lower frequency is termed as '1^{st} resonant response', while the other is termed as '2^{nd} resonant response'.

The FRF (magnitude) plots indicate that for changes in Φ and Q_{Total}, the frequency of the 1^{st} resonant response varies between 25 Hz and 40 Hz. With an increase in Φ, the peak of the 1^{st} resonant response becomes less pronounced indicating an increase in the its damping. Therefore, at the lower end of the frequency range, an increase in Φ causes a reduction in the FRF magnitude (also termed as the dynamic gain of the transfer function). This character of the 1^{st} resonant response is exhibited at all the flow rates studied. The frequency of the 2^{nd} resonant response increases significantly with increasing Φ, for all the total flow rates studied. This movement of the frequency of the 2^{nd} resonant response is primarily responsible for the broadening of the bandwidth of the FRF, which leads to higher FRF magnitudes at the upper end of the investigated frequency range. Based on the above discussion, it can be concluded that an increase in Φ adds damping at lower frequencies, and broadens the bandwidth of the flame dynamic response.

Figures 6.2, 6.4, 6.6, and 6.8 detail the phase of the FRF. These plots show that for lower values of Φ, there is a sharp drop in the phase at frequencies associated with the range of 1^{st} resonant response; beyond which the drop in phase is less pronounced. This behavior indicates the presence of lightly damped resonances at the low frequency range and no significant dynamic activity, due to lack of resonances at higher frequencies. With an increase

in Φ, the magnitude of the drop in phase around the lower frequency range is diminished which points to an increase in damping of the 1^{st} resonant response. Increase in Φ also decreases the drop in phase over the entire frequency range investigated. This indicates a broadening of the bandwidth, which has been attributed to the movement of the second resonant response to higher frequencies in the earlier discussion. At any particular fixed frequency of interest, within the range of 35-380 Hz, it is observed that an increase in Φ changes the phase of the FRF significantly. The change in phase is most pronounced in the frequency range of 35-100 Hz. The fore-mentioned observation could aid in the successful implementation of active control methodologies that are based on fluctuation in Φ.

To evaluate the influence of the flow rates on the FRF, the experimental data at $\Phi = 0.5$, and $\Phi = 0.75$ are plotted for all the flow rates in Figure 6.9 through Figure 6.12. Figures 6.9 and 6.11 show the magnitude of the FRF for $\Phi = 0.5$ and $\Phi = 0.75$ respectively, while Figures 6.10 and 6.12 show the phase of the FRF for $\Phi = 0.5$ and $\Phi = 0.75$ respectively. Both the magnitude and the phase plots indicate an increase in damping of the 1^{st} resonant response with an increase in Q_{Total}. This behavior is more pronounced at $\Phi = 0.5$, than at $\Phi = 0.75$. For both of these equivalence ratios, broadening of the bandwidth is observed with an increase in Q_{Total}, but the dependence of this phenomenon on Q_{Total} is not as pronounced as its dependence on Φ, as seen in Figure 6.1 through Figure 6.8. Figure 6.10 shows that with increase in Q_{Total}, the phase change at a particular frequency is significant in the frequency range of 35 to 90 Hz. Beyond 90 Hz, at any particular frequency the maximum difference in phase, due to the variation of flow rates is within 25 degrees. At $\Phi = 0.75$ (Figure 6.12), the phase could be loosely considered independent of the flow rates, because the variation in phase with the flow rate is within a narrow bandwidth of 25-40 degrees.

6.2.2 Physical Interpretation of the Experimental Results

In the previous section, the effects of Φ and Q_{Total} on the dynamic response of burner stabilized flat flames was discussed. This subsection correlates the experimental results to

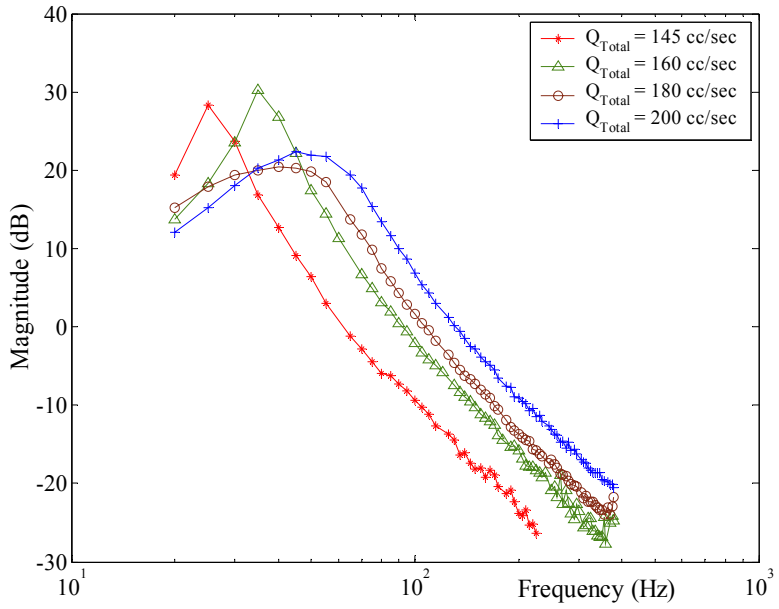

Figure 6.9: FRF (magnitude) for $\Phi = 0.5$ and methane-air mixture

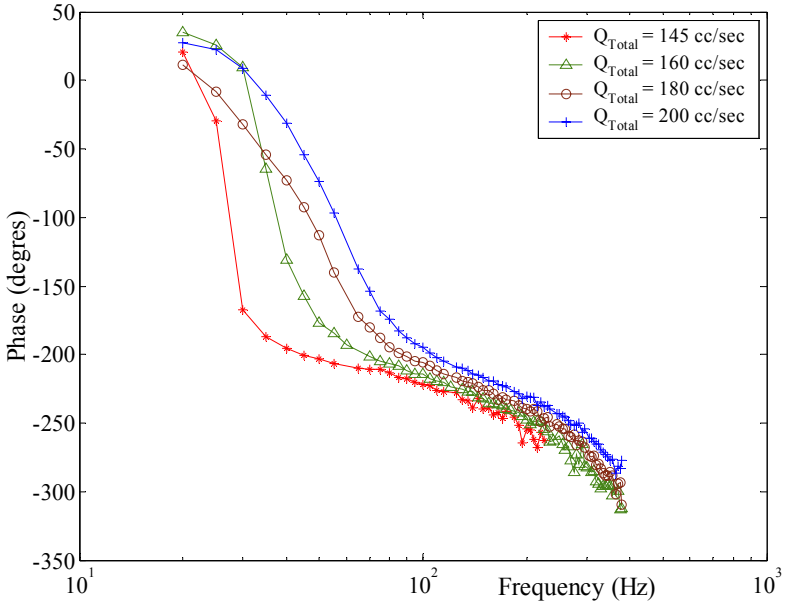

Figure 6.10: FRF (phase) for $\Phi = 0.5$ and methane-air mixture

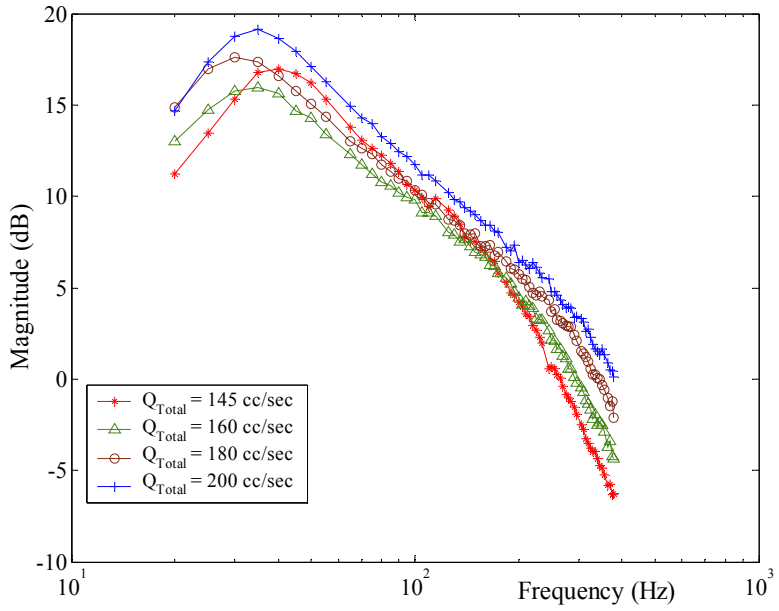

Figure 6.11: FRF (magnitude) for $\Phi = 0.75$ and methane-air mixture

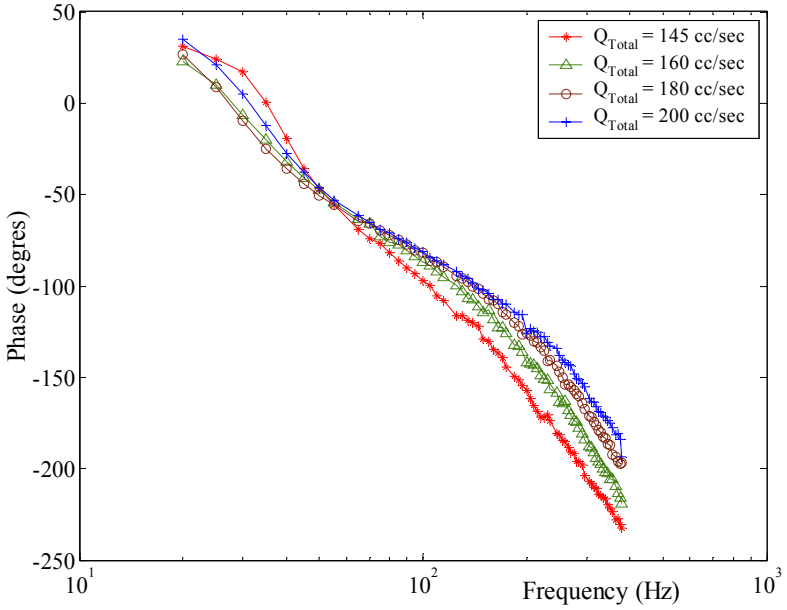

Figure 6.12: FRF (phase) for $\Phi = 0.75$ and methane-air mixture

Table 6.2: Percent change in the mean energy content for various flow conditions referenced to $\Phi = 0.5$ and $Q_{Total} = 145$ cc/sec

Total Flow Q_{Total} cc/sec	Equivalence Ratio (Φ)				
	0.5	0.55	0.6	0.65	0.75
145	0	9.82	18.89	27.87	46.9
160	10.97	20.29	30.54	40.27	60.76
180	22.83	35.62	47.68	57.58	80.53
200	36.82	50.49	63.77	76.05	100.75

the physics involved.

By increasing either Q_{Total} or Φ, the mean energy content of the reactant mixture is increased. Table 6.2 shows the percentage increase in the mean energy content of the reactant stream, for all of the experimental conditions studied using by $\Phi = 0.5$ and $Q_{Total} = 145$ cc/sec as the datum. Increasing Φ for a constant Q_{Total} generates a greater percentage increase in the mean energy content when compared to the percentage increase generated by an increase in the Q_{Total} for constant Φ. Therefore, the dependence of the mean energy content of the mixture is greater on Φ than on Q_{Total}. The conclusions in Section 6.2.1 were that the flame dynamics showed a greater dependence on Φ than on Q_{Total}, for changes in the damping characteristics of the 1^{st} resonant response. Therefore, based on the correlation of the two conclusions, an increase in mean energy content of the mixture contributes to the increased damping of the 1^{st} resonant response.

The broadening of the bandwidth of the dynamic response, primarily due to the movement of the 2^{nd} resonant response to higher frequencies is predominantly dependent on the Φ and is very weakly dependent on Q_{Total}. This trend indicates that the frequency of the 2^{nd} resonant response is dependent on a physical variable which is strongly effected by Φ and is almost independent of Q_{Total}. Reaction rate is one such physical variable. Ideally, under adiabatic conditions the reaction rate is only dependent on the equivalence ratio and is totally independent of the flow rate. Since in the present study, the flame was stabilized

under non-adiabatic conditions which were close to the adiabatic conditions, an increase in Q_{Total} can weakly effect the reaction rate by changing the flame temperature. The higher the equivalence ratio, the faster is the reaction. Therefore, an increase in the reaction rate can increase the frequency of the 2^{nd} resonant response and broaden the bandwidth of the overall dynamic response of the flame.

6.2.3 System Model

A reduced order model of the stable system that best matched the experimentally deduced FRF (both in magnitude and phase) was generated using the Controls Tool Box of Matlab. The modeling process started with assuming that the experimental data could be modeled with a pure time delay (τ), and an n^{th} order system. Here, the number of orders required to generate a stable model that accurately represented the data varied with each set of experimental data, but was never less than 8. The program essentially fitted the experimental data with a set of poles and zeros and a time delay with no consideration to the stability of the generated transfer function. Many a times, the high order transfer function generated was unstable, while the experimental data showed a stable system. In such cases, the generated model was stabilized by moving the unstable poles from the right half of the 's plane' to its left half, and correspondingly also moving equal amount of zeros from their existing position to the opposite half of the 's plane'. The new stabilized plant was then checked for its ability to predict the experimental FRF. If the stabilized high order model does not accurately predict the experimental FRF, the process of obtaining a stabilized model described above was iterated upon either by changing the order of the initial guess or by moving a different set of zeros in the stabilizing process.

Once a high order stabilized model that accurately represents the experimental data was obtained, its states were characterized based on their observability and the controllability characteristics This process essentially quantified the influence of the various states on the behavior of the model. The order of the model was then reduced by removing the states that

had the least influence without adversely effecting the accuracy of the model prediction. This process was continued until the lowest possible order was achieved. All the models showed that the burner stabilized laminar flat flame behaves as a fourth order system, with a pure time delay.

Therefore, the transfer function has the following form.

$$TF = \frac{K_1\, e^{-s\tau}\, N(s)}{(s^2 + 2\,\zeta_1\,\omega_{n1}\,s + \omega_{n1}^2)(s^2 + 2\,\zeta_2\,\omega_{n2}\,s + \omega_{n2}^2)} \tag{6.1}$$

where ω_{n1} and ω_{n2} are two natural resonant frequencies, N(s) is polynomial containing the zeros which may be real or complex, K_1 is the gain, τ is the time delay, and ζ_1 and ζ_2 are the damping ratios.

The model prediction for each of the data sets are plotted over their respective experimental data in Figure 6.1 to Figure 6.8. The models replicate the experimental data fairly well, except for a small deviation in the magnitude of Q_{Total} = 160 cc/sec and Φ = 0.5, at the higher end of the frequency range. The models generated parameters; poles, zeros, gain and τ are tabulated in Appendix D.

For each set of experimental data, the model generates two sets of complex conjugate poles, each of which is responsible for one resonance. As described in section 6.2.1, the resonances are defined as the 1^{st} resonant response and the 2^{nd} resonant response. For all the experimental conditions being studied, the models predict the 1^{st} resonant response to be in the frequency range of 20.5 to 37.2 Hz and the 2^{nd} resonant response to be in the frequency range of 23.4 to 240.5 Hz. The 1^{st} and the 2^{nd} resonances for all the data are plotted on the complex plane in Figure 6.13 and Figure 6.14 respectively. The damped natural frequency axis of the complex plane has a damping ratio (ζ), of 1, while the resonant frequency axis has $\zeta = 0$. The plots clearly indicate that an increase in Φ, or in Q_{Total} increases ζ of the 1^{st} resonant response. The 2^{nd} resonant response follows two distinct ζ lines with the transition occuring between Q_{Total} = 160 cc/sec, Φ = 0.55 (-24.96, $\pm$69.79) and Q_{Total} = 160 cc/sec, Φ = 0.6 (-58.01, $\pm$98.01). The movement of the 2^{nd} resonant response to higher resonant frequencies with increase in Q_{Total} and Φ is far more rapid compared to the 1^{st} resonant

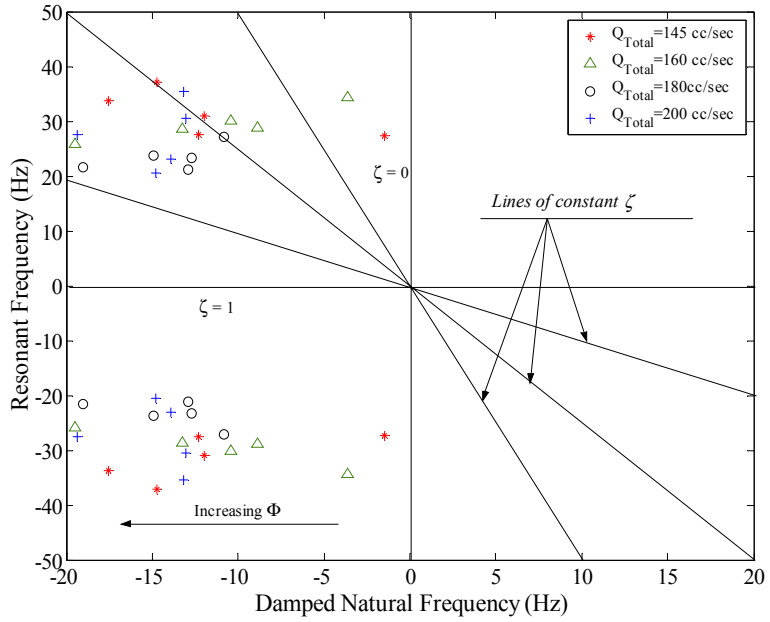

Figure 6.13: Phase plane for the 1^{st} resonant response, methane-air mixture

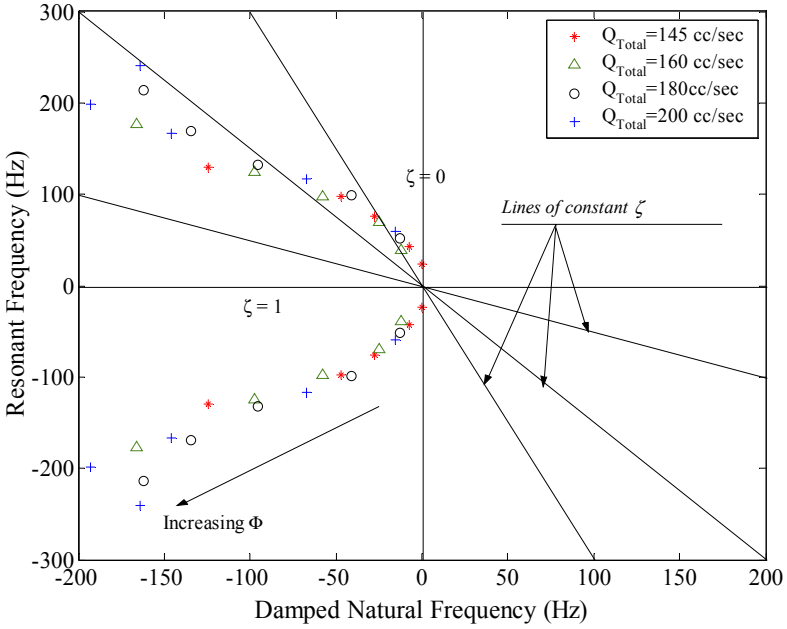

Figure 6.14: Phase plane for the 2^{nd} resonant response, methane-air mixture

response.

6.2.4 1^{st} Resonant Response

The 1^{st} resonant response defined in Section 6.2.3, varies within a small range of resonant frequency for changes in the mean energy content of the incoming reactant mixture. However, its damping increases considerably with an increase in the mean energy content of the reactant mixture. This behavior of the 1^{st} resonant response inclined the author to believe that its physics was linked to the fluctuations in the energy exchange between the flame front and the honeycomb. Such energy exchange oscillations are expected to vary the flame temperature and hence, the flame speed in a periodic manner.

To investigate the above hypothesis in greater depth, the signal from the 'Type R' thermocouple imbedded on the top surface of the honeycomb was analyzed. In most of the cases, the 'Type R' thermocouple exhibited a measurable dynamic response within the frequency range of 20-70 Hz. This can be verified from Figure 6.15, which shows the coherence between the 'Type R' thermocouple signal and u', indicating that in the range of 20-70 Hz the temperature of the top of the honeycomb oscillates at the same frequency as that of the induced velocity fluctuations. Since the amplitudes of these fluctuations were fairly small and the bandwidth of the thermocouple response is not expected to exceed 160 Hz, the coherence beyond 70 Hz is generally poor.

The measured dynamic response of the thermocouple is indicative of a fluctuation in the net energy absorbed by the honeycomb. Such fluctuations in the net energy absorbed by the honeycomb could be generated due to oscillations in the net energy exchange between the honeycomb and the flame front, or between the honeycomb and the reactant stream flowing through the honeycomb channels.

The oscillatory heat exchange between the honeycomb and the reactants could only be generated by an oscillation in the convective heat transfer coefficient at the channel walls of the honeycomb, due to presence of a fluctuating flow velocity. As the characteristic dimension of

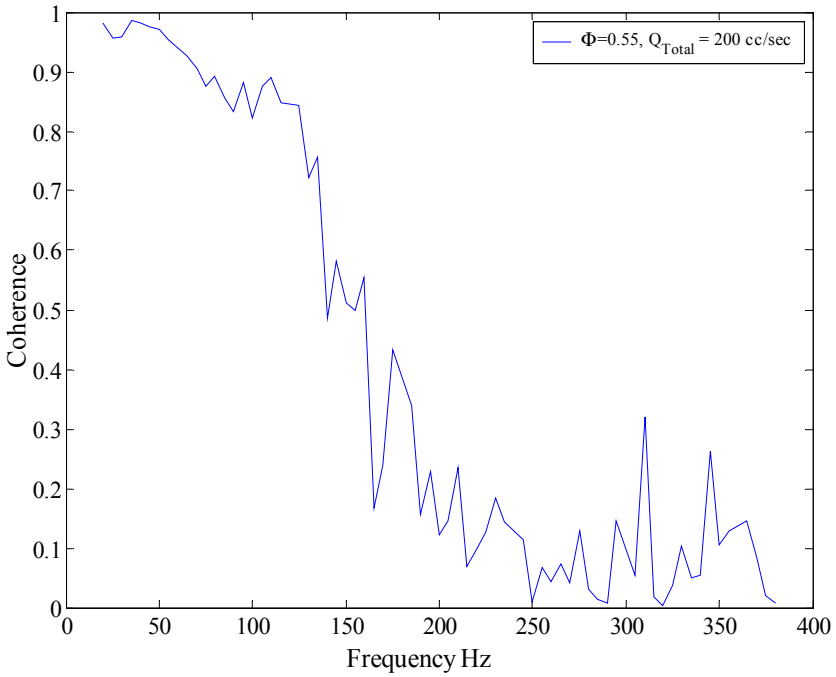

Figure 6.15: Coherence between the 'Type R' thermocouple signal and u'

each of the honeycomb channel is at least 18 times smaller than the axial length along the direction of the flow, and the flow being laminar, the thermal and the hydrodynamic boundary layers within the honeycomb channels are expected to be fully developed at its downstream end. However, both the hydrodynamic and the thermal boundary layers are expected to be simultaneously developing between the inlet of the honeycomb and its top surface. The local convective heat transfer coefficient, (h_x), for such a simultaneously developing flow has been studied extensively and is well documented in literature [1]. The studies show that the non-dimensionalized local heat transfer coefficient, the 'Nusselt Number' $(Nu_{x,H})$, depends on the nondimensionalized axial distance of the location x^* from the leading edge and on Prandtl Number, (Pr). This is graphically shown in Figure 6.16.

Here x^* is given by

$$x^* = \frac{\frac{x}{D_h}}{Re\, Pr} \tag{6.2}$$

For the entire range of parameters in the present study, x^* as calculated at the top surface

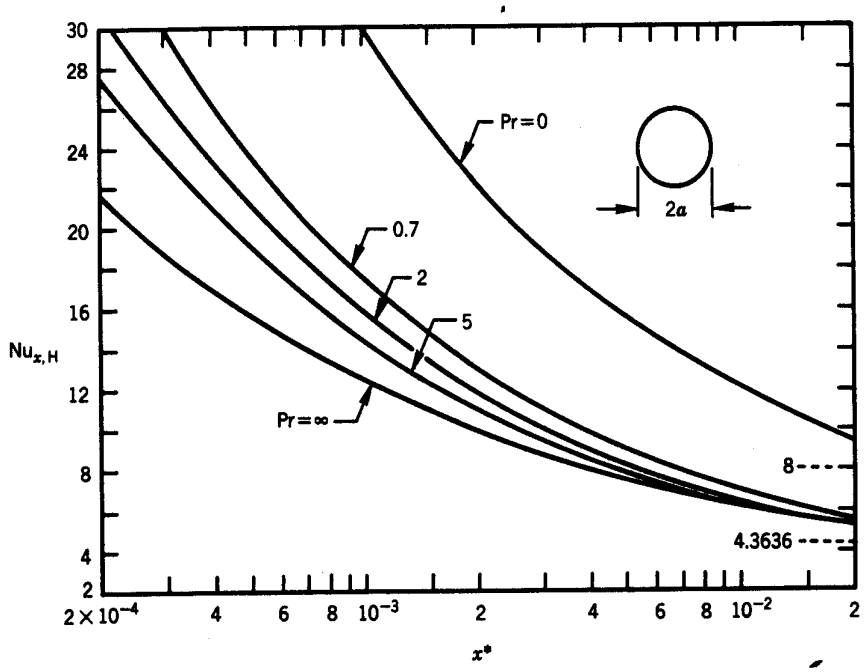

Figure 6.16: Local Nusselt numbers for simultaneously developing flow in a circular duct [1]

of the honeycomb ranges from 9.26 to 15.34. This entire range of x^* is far greater than the value of 0.02, beyond which the flow is expected to be fully developed both thermally and hydrodynamically. The fully developed conditions predicted by $x^* = 0.02$ are reached well within a distance of 0.05 mm from the inlet of the honeycomb. Therefore, based on the Figure 6.16, the heat transfer coefficient is independent of the flow parameters. Thus, small perturbations in the velocity of the order of 1 to 2 % of the mean flow velocity are not expected to change the local heat transfer coefficient near the top surface of the honeycomb. Therefore, the oscillations in the net energy absorbed by the honeycomb is almost independent of the flow oscillations in its channels. Hence, the dynamic response of the honeycomb is primarily due to the fluctuation of net heat transfer from the flame via radiative and conductive modes.

The fore-mentioned conclusion is also proven by modeling the FRF of the dynamic signal from the 'Type R' thermocouple to u' in the frequency range where reasonable coherence is exhibited. Figure 6.17 and Figure 6.18 respectively show the magnitude and the phase

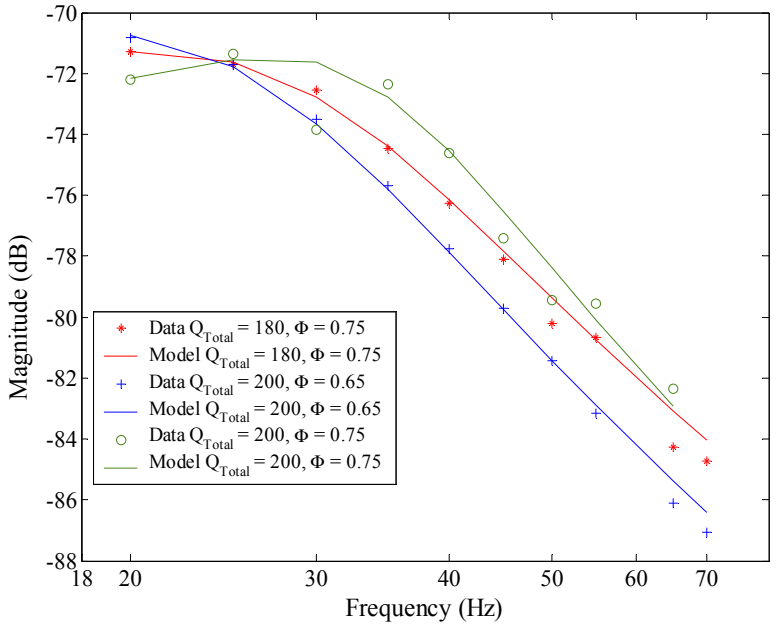

Figure 6.17: FRF (magnitude) of the 'Type R' thermocouple signal and u' for methane-air mixture

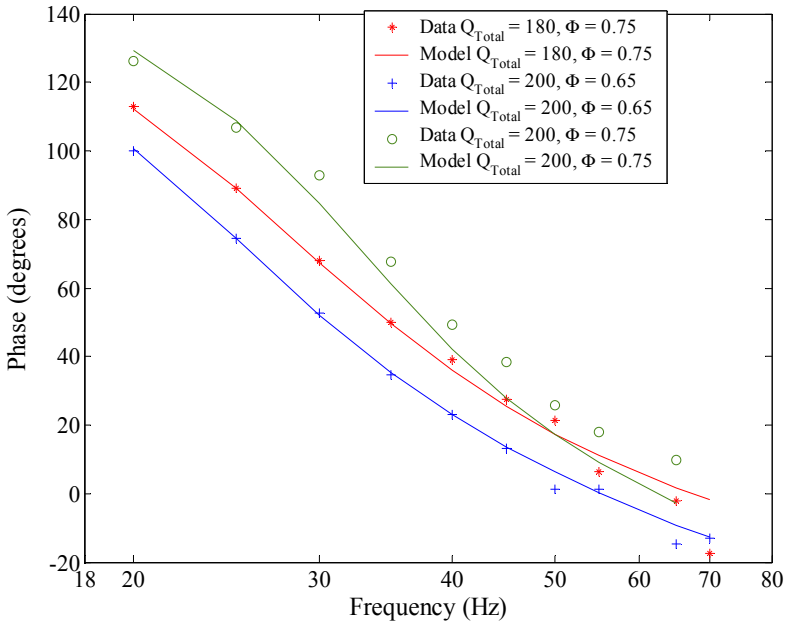

Figure 6.18: FRF (phase) of the 'Type R' thermocouple signal and u' for methane-air mixture

Table 6.3: Resonant frequencies of the 1^{st} resonant response compared with the resonances evaluated for the thermocouple dynamics

Total Flow Q_{Total} (cc/sec)	Equivalence Ratio (Φ)	1^{st} Resonant Response (Hz)	Thermocouple Dynamic Resonance (Hz)	Ratio of column 3 to column 4
145	0.6	27.64	27.42	1.01
160	0.55	28.92	28.85	1.00
160	0.75	25.76	27.16	0.95
180	0.5	27.08	29.84	0.91
180	0.55	23.24	21.81	1.07
180	0.6	21.15	20.45	1.03
180	0.65	23.66	20.8	1.14
180	0.75	21.65	24.05	0.90
200	0.5	35.45	32.69	1.08
200	0.55	30.57	32.08	0.95
200	0.6	23.06	22.4	1.03
200	0.65	20.47	21.36	0.96
200	0.75	27.56	29.67	0.93

of the FRF and the corresponding models for few of the cases evaluated. Although, all the experimental data sets were evaluated, models for only a few are shown in Figure 6.17 and Figure 6.18 for the purpose of discussion. The procedure used for developing the models was identical to that described in Section 6.2.3. The resulting resonant frequencies predicted by the models and the frequencies of the corresponding 1^{st} resonant response are tabulated in Table 6.3. This Table also shows the ratio of the two frequencies. The value of the ratio being almost unity for all the conditions indicates that the two resonances are at the same frequency. Such a situation can arise only if the two signals from the OH^* chemiluminescence and the 'Type R' thermocouple are dependent on each other. Therefore, it can be conclusively said that the fluctuations in the temperature of the honeycomb are primarily due to the fluctuations in the dynamic heat exchange between the flame front and the honeycomb top surface.

The net heat transfer fluctuation from the flame can only be caused by an oscillatory flame temperature, thus indicating a fluctuation in flame speed, (S_L). Assuming the flame front

to be totally flat and one dimensional in nature, this S_L fluctuation causes the flame front to oscillate axially about its mean position above the honeycomb. With increase in the mean energy content of the fresh fuel-air mixture, the mean flame temperature rises, thus increasing the potential to transfer energy to the honeycomb. Consequently the heat transfer coupling that anchors the flame to the honeycomb becomes stronger. Therefore, at conditions with higher mean energy and enhanced heat transfer potential, most of the fluctuations in the dynamic heat release due to oscillations in the velocity of the reactant stream are re-circulated back to the honeycomb. This leads to damping of the fluctuations in the mean energy content of the products of combustion, which results in damping of the oscillation in the flame temperature. Thus, there is significant reduction in the amplitude of oscillation of S_L and hence the oscillation of the flame about its mean position. Therefore, with an increase in mean energy content of the fresh fuel-air mixture, the system is expected to exhibit a higher ζ.

Conduction is one of the modes of transferring energy from the flame to the honeycomb, and $\frac{dT}{dx}$ can be considered as a measure of the potential for the net heat transfer between the flame front and the honeycomb. Assuming a one dimensional system, the conductive heat transfer between the flame front and the honeycomb is given by

$$q_{net} = k\, A_c \frac{dT}{dx} \tag{6.3}$$

where k is the thermal conductivity of the gas, A_c is the cross sectional area of the flow, and $\frac{dT}{dx}$ is the spatial temperature gradient between the flame front and the honeycomb.

Therefore,

$$q_{net} \propto \frac{dT}{dx} \tag{6.4}$$

The estimation of $\frac{dT}{dx}$ was obtained by modeling each of the test conditions in 'Burner Stabilized Premix' [75] that is discussed in Section 6.2.5. $\frac{dT}{dx}$ was approximated using finite differences as

$$\frac{dT}{dx} \approx \frac{T_{OH^*} - T_b}{X_{OH^*} - X_b} \tag{6.5}$$

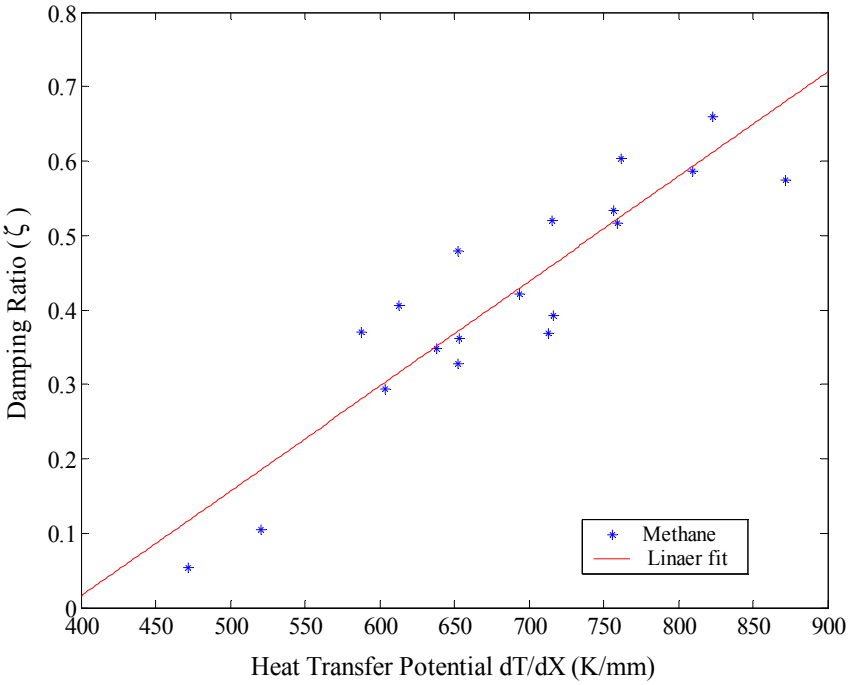

Figure 6.19: Dependence of ζ of the 1^{st} resonant response on the heat transfer potential

where T_{OH^*} is the temperature of the reacting flow at a spatial location X_{OH^*} where the mole fraction of the OH^* species, as modeled by 'Premix' is maximum. T_b is the temperature of the top surface of the honeycomb as measured by the 'Type R' thermocouple. X_b is the spatial position where T_b was measured. Both X_{OH^*} and X_b are referenced to the inlet of the computational domain, which in the present case is the top surface of the honeycomb. Therefore $X_b = 0$. Based on the above definitions, the $\frac{dT}{dx}$ evaluated using equation 6.5 has units of Kelvin/mm.

ζ of the 1^{st} resonant response is plotted as a function of $\frac{dT}{dx}$ in Figure 6.19, which shows that the ζ increases linearly with an increase in potential for q_{net}, thus confirming the discussion of the 1^{st} resonant response. Therefore, eventually it can be concluded that the 1^{st} resonant response exhibited by the system is indicative of the fluctuations in the flame speed and is strongly effected by the heat transfer coupling between the flame and the burner dynamics.

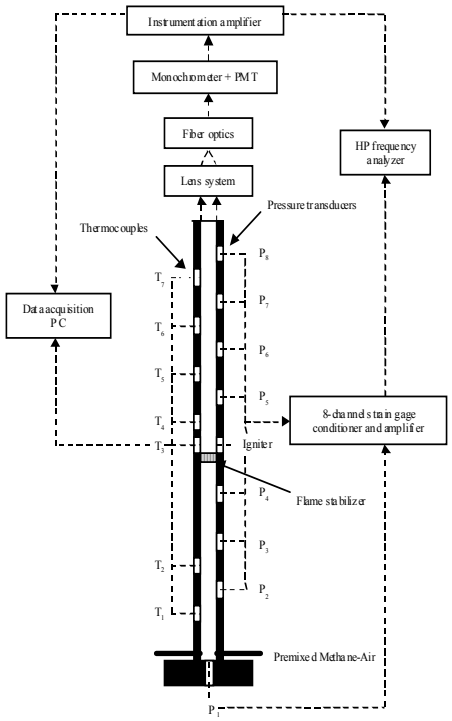

Figure 6.20: Sketch of the Rijke tube combustor

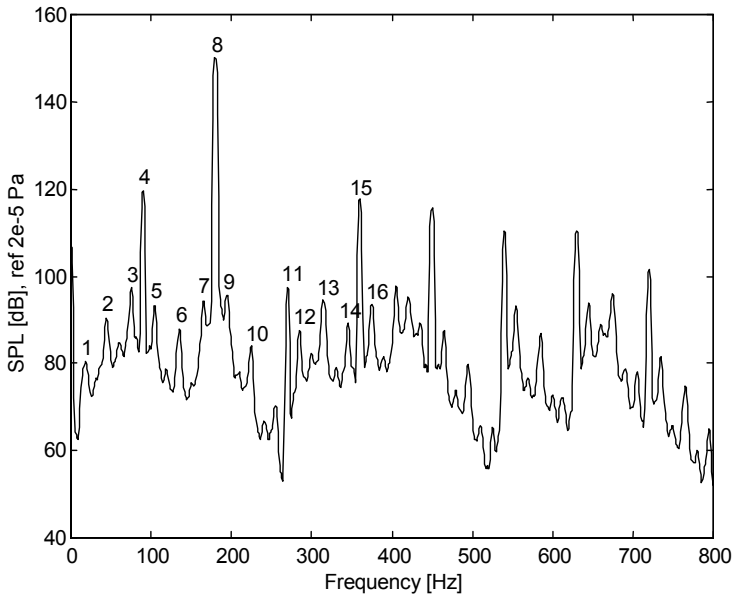

Peak - Description
1 - pulsating instability
2 - $f_{LC}/4$
3 - lower AM sideband
4 - subharmonic ($f_{LC}/2$), $2f_{LC}/4$
5 - upper AM sideband
6 - $3f_{LC}/4$
7 - lower AM sideband
8 - f_{LC}, TA instability
9 - upper AM sideband
10 - $5f_{LC}/4$
11 - $3f_{LC}/2$, $6f_{LC}/4$
12 - upper AM sideband
13 - $7f_{LC}/4$
14 - lower AM sideband
15 - $2f_{LC}$, $4f_{LC}/2$, $8f_{LC}/4$
16 - upper AM sideband

Figure 6.21: Typical power spectrum of the pressure trace for the Rijke tube combustor

Figure 6.20 shows the sketch of a Rijke tube combustor studied by Nord [76] and also reported by Saunders et al. [51]. The Rijke tube combustor consists of a $2\frac{1}{2}$" diameter steel pipe that is 5 feet long, closed at the bottom end and opened at the top. Its design is such that the combustion process is expected to satisfy Rayleigh's criteria and the system is expected to exhibit thermo-acoustic instabilities. A typical power spectrum of the pressure trace for this tube is shown in Figure 6.21. The power spectrum exhibits amplitude modulating side bands around the limit cycle frequency, with a frequency corresponding to the first peak in the power spectrum. It is proposed that the 1^{st} resonant response is responsible for these amplitude modulating side bands. Therefore, apart from being a low frequency thermo-diffusive oscillation, the 1^{st} resonant response directly impacts the thermo-acoustic instability in a combustion process by modulating its amplitude.

Since the 1^{st} resonant response is primarily driven by the energy interaction between the flame and its surroundings, the author expects that these resonances would also be present in both turbulent flames having flamelet regimes and well stirred reactor volumes. Thus, these low frequency resonances must be sought and accounted for while developing sub-harmonic control algorithms that are designed to actively control the thermo-acoustic instabilities through a control signal at a low frequency.

6.2.5 2^{nd} Resonant Response

In Section 6.2.2, it was proposed that the 2^{nd} resonant response was primarily dependent on the reaction rate of a combustion process. To prove this deduction, the resonant frequency of the 2^{nd} resonant response must be correlated to the reaction rate, which is given by the Arrhenius expression

$$RR = A\,[OX]^n\,[F]^m\,\exp\frac{-Ea}{Ru\,T} \tag{6.6}$$

where RR is the reaction rate, A is the pre-exponential factor, [OX] and [F] are the concen-

trations of the oxidizer and fuel respectively, Ea is the activation energy, R_u is the universal gas constant, and T is the reaction temperature.

For a combustion process involving 'j' species (including reactants, products and intermediate) and 'p' elementary reactions, there are 'p' reaction rates that are coupled. Thus, the combustion process is equivalent to a p^{th} order dynamic system, of which there may be a few dominant modes. Typically all the 'p' modes of such a system would have their frequencies varying exponentially with temperature, as is exhibited by equation 6.6. Thus, to prove the hypothesis, it was decided to compare the resonant frequency of the 2^{nd} resonant response to the flame temperature.

'Burner Stabilized Premix' [75], a code written by Sandia labs to model laminar premixed flames with detailed finite reaction rate chemistry, was used to model the burner stabilized laminar flat flame and evaluate the flame temperature. While modeling with 'Premix', the option of burner stabilized modeling was activated and the burner temperature was fixed to the temperature measured by the 'Type R' thermocouple. A detailed mechanism file, GRI. Mec III [77] was modified to include OH^* mechanism [70]. This modified mechanism was used to evaluate the mole fraction of the OH^*. Each of the experimental condition was simulated and the maximum temperature was recorded as the flame temperature, (T_f). The resonant frequency of the 2^{nd} resonant response was plotted as a function of the evaluated flame temperature, and is shown in Figure 6.22.

It is observed that the resonant frequency of the 2^{nd} resonant response varies exponentially with the flame temperature, for all the equivalence ratios up to $\Phi = 0.65$. The results for $\Phi = 0.75$ do not lie on the exponential fit. This deviation from the rest can be attributed to the fact that the flame temperature calculated using 'Premix' was not totally accurate. 'Premix' models the reacting flow based on the temperature profile and the species profile. For the purpose of this analysis, the inlet boundary conditions of the computational domain defines the incoming mixture to consist of only the fuel and oxidizer species, and the inlet fluid temperature to be equal to the experimentally measured temperature of the top surface

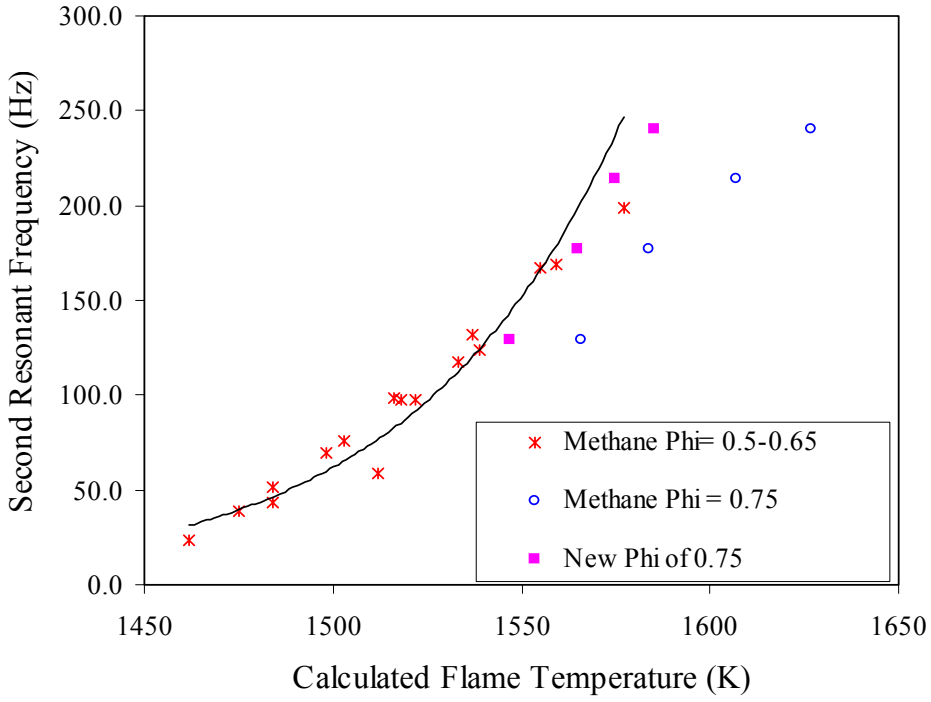

Figure 6.22: Frequencies of the 2^{nd} resonant response plotted as a function of flame temperature

of the honeycomb. For the experimental conditions where $\Phi = 0.75$, the temperature at the top surface of the honeycomb was well above the ignition temperature (Table 6.1). Thus, physically the reaction had started within the honeycomb. Therefore, the species composition of the mixture at the top surface of the honeycomb is different from the modeled composition of the pure reactants. This effects the accuracy of the predicted flame temperature. However, if these temperature estimates were reduced by about 2%, the results of $\Phi = 0.75$ would also lie on the exponential fit.

It is well accepted that for combustion of methane there is a threshold temperature below which the dominant reactions contributing towards heat release are quite different from those that contribute towards heat release at temperatures above the threshold temperature. Furthermore, based on their dynamic characteristics, each of these dominant sets of reactions is expected to have a characteristic ζ, which remains constant for small variations in the flame temperature. Therefore, as long as a particular set of reactions dominates the heat release

mechanism, ζ of the chemical kinetics should remain almost constant. The 2^{nd} resonant response reflects this behavior as seen in Figure 6.18. There is a significant change in ζ as we move from $\Phi = 0.55$ to $\Phi = 0.6$. Below $\Phi = 0.55$ and above $\Phi = 0.6$, ζ remains fairly constant.

Thus, the 2^{nd} resonant response represents the reduced order kinetic model that captures all of the important dynamic characteristics of finite rate chemistry. Therefore, while modeling reacting flows, if the dynamics of the chemical kinetics are important and need to be studied, then the use of at least a two step chemical kinetic model having a minimum of two reaction rates is advised.

6.2.6 Time Delay

The models generated from the experimental data showed the behavior of the flame dynamics to be fourth order in nature with a time delay. Discussions in Section 6.2.4 and Section 6.2.5 correlated the two resonances to the physics involved. Similarly, the time delay used in the modeling needs to be associated with a physical phenomenon occurring in the dynamics of the combustion process.

Since acoustically a standing wave is generated within the rig, there is no phase change between the plane of u' measurement and the flame front. Therefore, there is no time delay due to the acoustics of the rig. The only time delay, τ, that can occur in the present experiment is the delay between the u' that is felt at the flame front and the corresponding q' signal. This delay is due to the finite rate chemistry of the combustion process.

This time delay, τ_{chem} was evaluated using the results of 'Burner Stabilized Premix' modeling, discussed in Section 6.2.5. τ_{chem} was defined to be the time required to move the fluid within the flame front from the point at which OH* mole fraction was 10% of the maximum, to the point at which the maximum occurred.

The τ_{chem} thus predicted and that calculated by the modeled fits are plotted as a function of

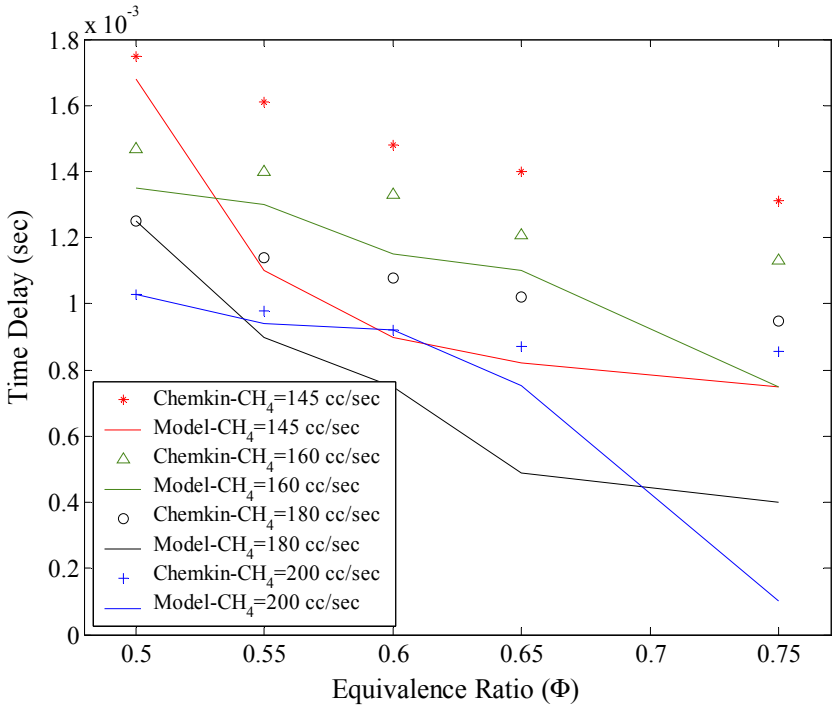

Figure 6.23: Time delay as a function of Φ for methane-air mixture

Φ and Q_{Total} in Figure 6.23. The time delay used to generate reduced order models compares well with the predictions of time delay made using the 'Premix' code. In most cases, the difference between the predicted and the modeled delay is within a deviation of 30 %, except for cases with $\Phi = 0.75$, and also for cases with $Q_{Total} = 145$ cc/sec.

The constant delay used in the dynamic model prediction is part of a dynamic process, while the predicted delay is based on computation of a steady state problem. In reality, the time delay as has been defined in this problem will vary as the reaction rates fluctuate during a perturbation cycle, thus causing small changes in the thickness of the reaction zone. By using a constant time delay, the mean part of the actual delay has been accounted, while the fluctuating component was incorporated in the dynamic description of the reduced order model (i.e within the poles and zeros of the system). Furthermore, the constant time delay used in the dynamic model prediction, in itself could be a simplification of the higher order dynamics, which are not accounted in τ_{chem}.

Considering this background, the deviation of 30 % between the two evaluations seems quite reasonable. Greater than 30 % deviation for $\Phi = 0.75$ could be attributed to the deficiency in the 'Premix' modeling process as discussed earlier in Section 6.2.5. The discrepancy in the results for a $Q_{Total} = 145$ cc/sec could be associated with the fact that at lower flow rates the oscillations in the reaction rates may be more significant. The combustion process itself is inherently non-linear (although we are approximating a linearized plant), the unequal excursion about the mean delay would lower the effective mean delay that is used in the generation of reduced order models, while the delay calculated by 'Premix' remains unchanged.

However, if the reader would prefer to use the τ_{chem} instead of τ, then the drift in phase, θ^*, is given by

$$\theta^* = -2\pi f(\tau_{chem} - \tau) \tag{6.7}$$

where f is the frequency in Hz. The corresponding phase would then be

$$\theta = \theta_{expt} + \theta^* \tag{6.8}$$

6.3 Experimental Results of Propane and Ethane Combustion

The analysis of the laminar flame dynamic experiment using methane-air mixtures showed that the flame speed oscillations and the chemical kinetics defined the dynamic behavior of the laminar flat flame. Furthermore, both these physical effects generate resonances in a bandwidth of 20 to 250 Hz and thus can significantly effect the thermo-acoustic instabilities experienced by the combustion systems, by altering both the magnitude and the phase of the dynamic heat release. Therefore, it is expected that changing the fuel will alter the dynamic behavior of the combustion process and hence, the manifestation of thermo-acoustic instabilities.

To evaluate the effects of the other major components of natural gas, experiments were

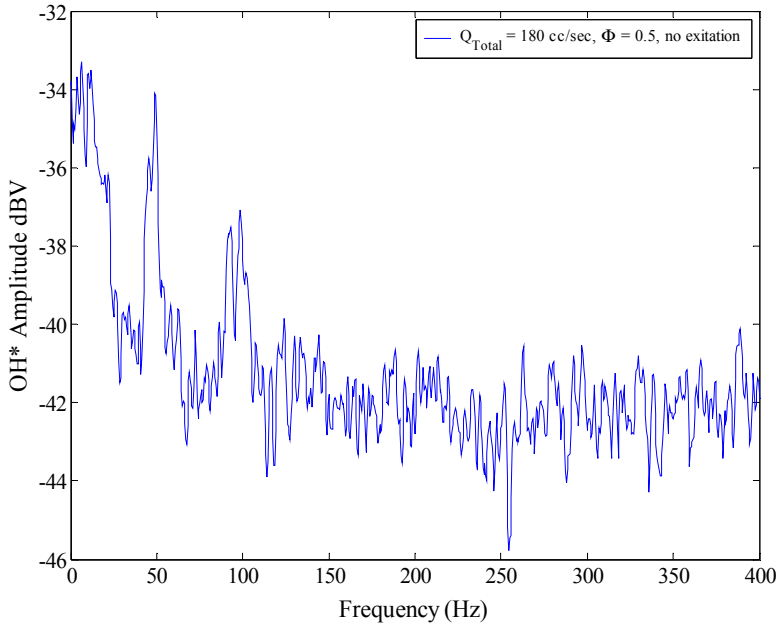

Figure 6.24: Power spectrum of the OH^* signal at $Q_{Total} = 180$ cc/sec, $\Phi = 0.5$ and no external excitation for propane-air flames

conducted with both propane and ethane. Section 6.3.1 describes and discusses the results of propane-air experiments, while Section 6.3.2 discusses the results of experiments conducted with ethane-air mixture.

6.3.1 Dynamics of Propane-air Flames

Experiments were conducted with bottled instrument grade propane for five equivalence ratios ranging from 0.52 to 0.75, and for four flow rates ranging from 145 cc/sec to 200 cc/sec. The parametric conditions were chosen to be the same as those studied for methane-air experiments primarily to be able to compare the results. However, $\Phi = 0.5$ could not be studied as the combustion was dynamically unstable, inspite of having a stable burning flame from the blowoff or flashback point of view. Therefore, it was impossible to accurately analyze the linearized flame dynamics. The dynamic instability can be clearly seen in Figure 6.24, which shows the power spectrum of the OH^* for $Q_{Total} = 180$ cc/sec and $\Phi = 0.5$.

No external excitation was provided, yet there are distinct peaks at 50 and 100 Hz, which are later on shown to be due to the movement of the 2^{nd} resonant pole to the right half of the 's plane', thus making the system unstable. $\Phi = 0.52$ was the lowest dynamically stable equivalence ratio that could be achieved and studied.

Figure 6.25 through Figure 6.32 show the magnitude and the phase of the FRF between the OH^* chemiluminescence signal and the u', for the four flow rates starting with 145 cc/sec and ascending to 200 cc/sec. Both the magnitude and the phase plots of the FRF indicate similar characteristics as seen for methane-air flames described in Section 6.2.1. The dynamic system exhibits characteristics of a fourth order system with the 2^{nd} resonant response being primarily responsible for the broadening of the bandwidth as the Φ is increased. The movement of the resonant frequency of the 1^{st} resonant response with changes in Φ and Q_{Total} is limited to the range of 35 to 50 Hz. However, with increase in Φ, the 1^{st} resonant response exhibits significant increase in damping.

The entire set of experimental data for the dynamics of propane-air flames was modeled using the procedure described in Section 6.2.3. The results show that the dynamics of premixed propane-air laminar flat flames behave as a fourth order system with a pure time delay. The predictions of the models are plotted over the respective experimental data set in Figure 6.25 through Figure 6.32. The model predictions match the data very well, except for the magnitude at the flow condition of 145 cc/sec and $\Phi = 0.55$, at the higher end of the frequency range. The model generated parameters; poles, zeros, gain and τ are tabulated in Appendix D.

Consistent with the definitions used in the analysis of methane-air flames, the two resonances obtained from the models were termed as '1^{st} resonant response' and '2^{nd} resonant response', and are plotted on the 's plane' in Figure 6.33 and Figure 6.34 respectively. The first resonant response is limited to the frequency range of 20-45 Hz and shows significant increase in damping with increase in the mean energy content of the mixture. The damping ratio was therefore plotted as a function of $\frac{dT}{dx}$, the potential to transfer energy from the flame to the

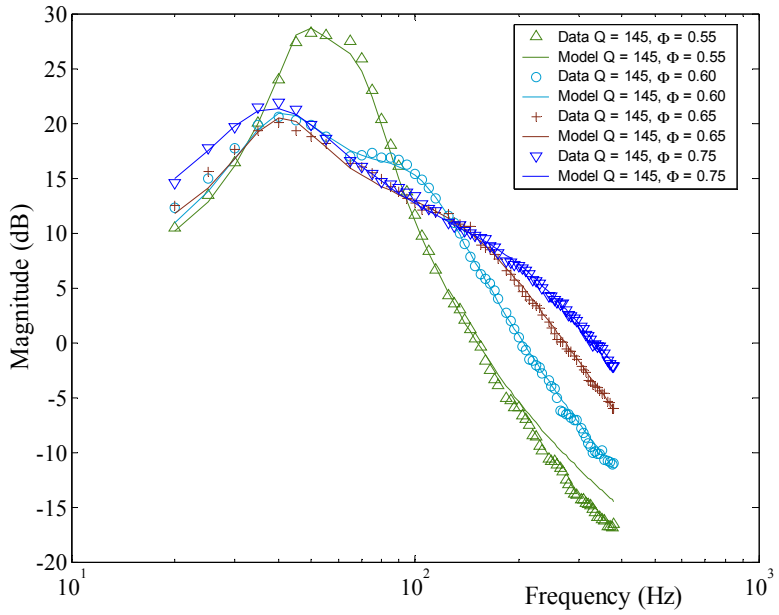

Figure 6.25: FRF (magnitude) for $Q_{Total} = 145$ cc/sec and propane-air mixture

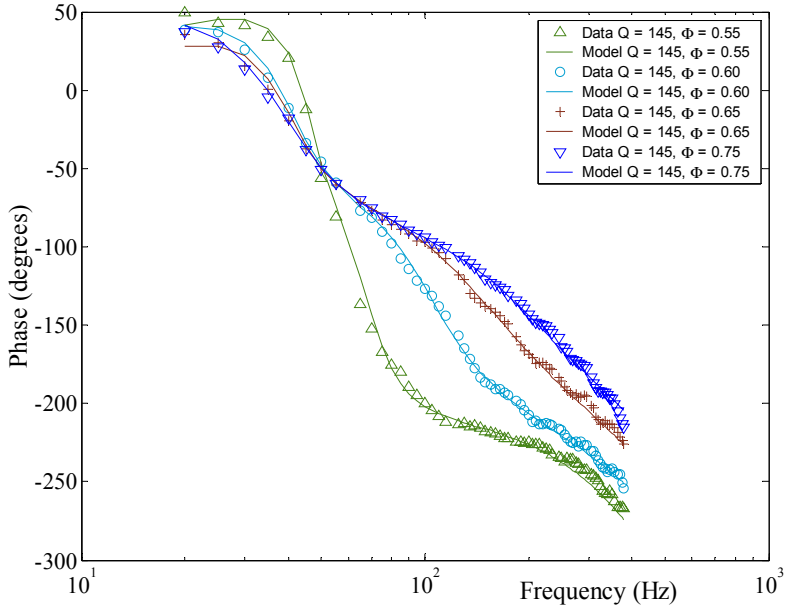

Figure 6.26: FRF (phase) for $Q_{Total} = 145$ cc/sec and propane-air mixture

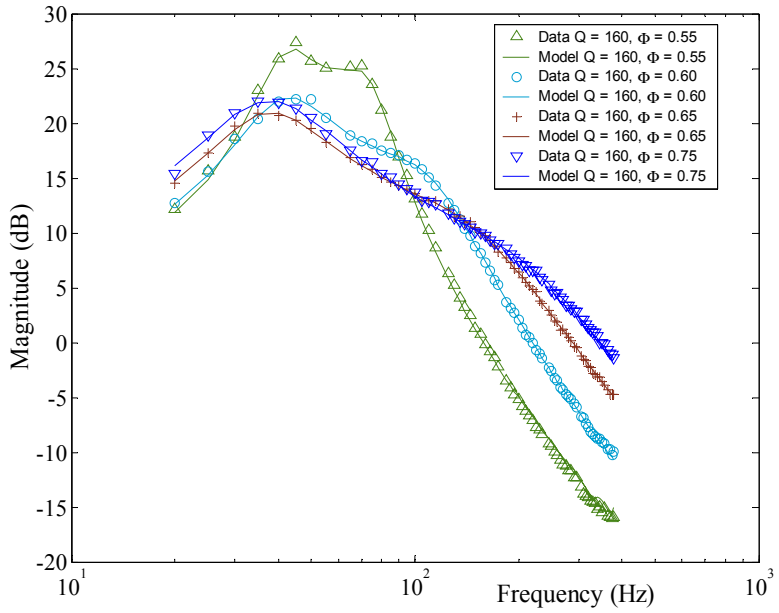

Figure 6.27: FRF (magnitude) for $Q_{Total} = 160$ cc/sec and propane-air mixture

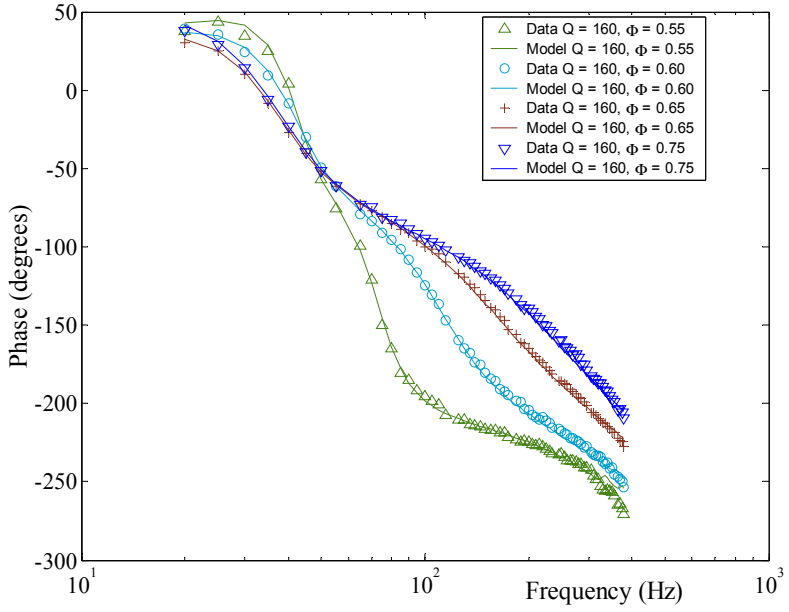

Figure 6.28: FRF (phase) for $Q_{Total} = 160$ cc/sec and propane-air mixture

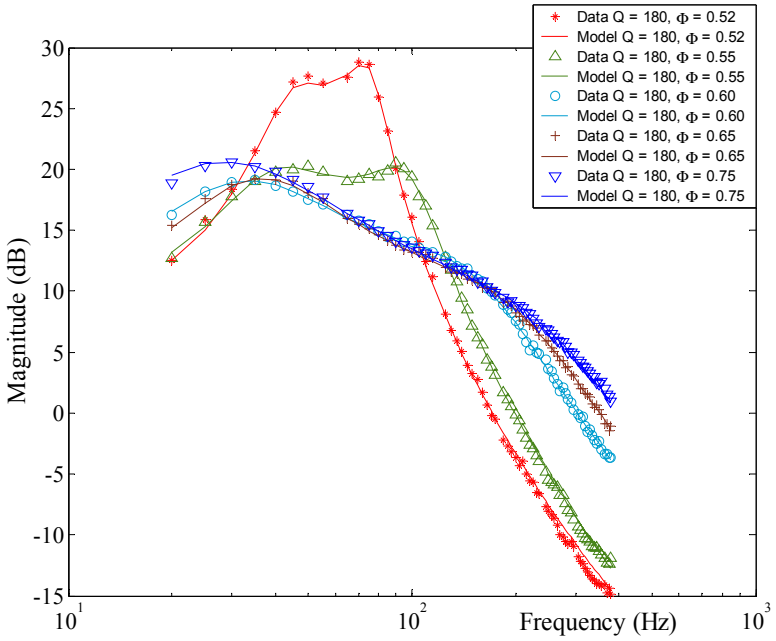

Figure 6.29: FRF (magnitude) for $Q_{Total} = 180$ cc/sec and propane-air mixture

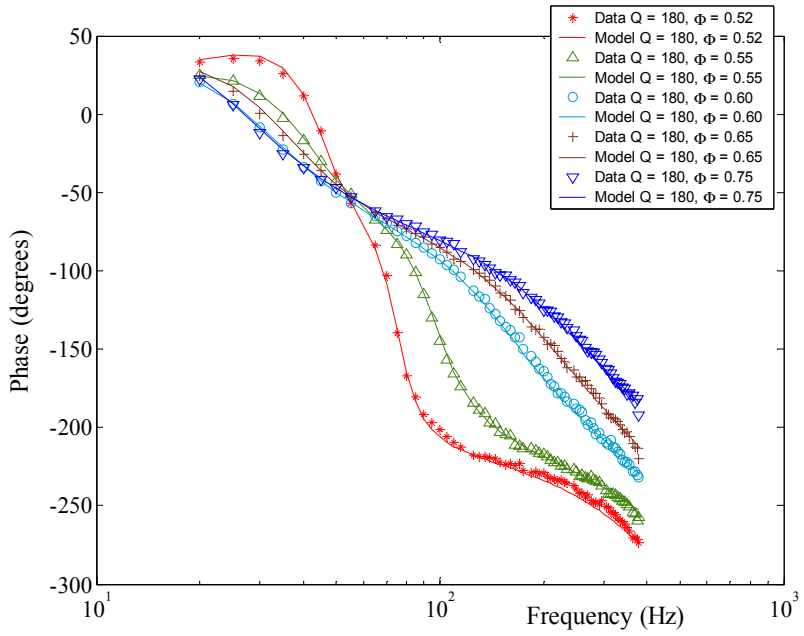

Figure 6.30: FRF (phase) for $Q_{Total} = 180$ cc/sec and propane-air mixture

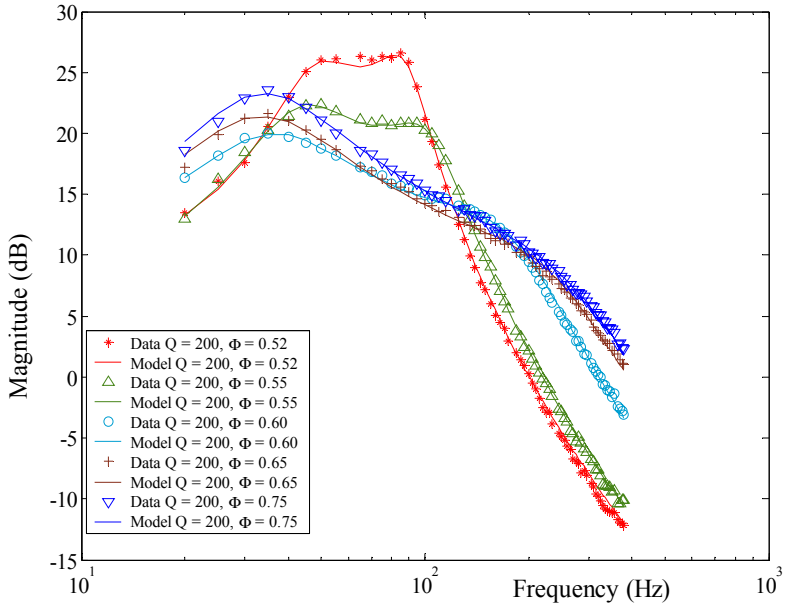

Figure 6.31: FRF (magnitude) for $Q_{Total} = 200$ cc/sec and propane-air mixture

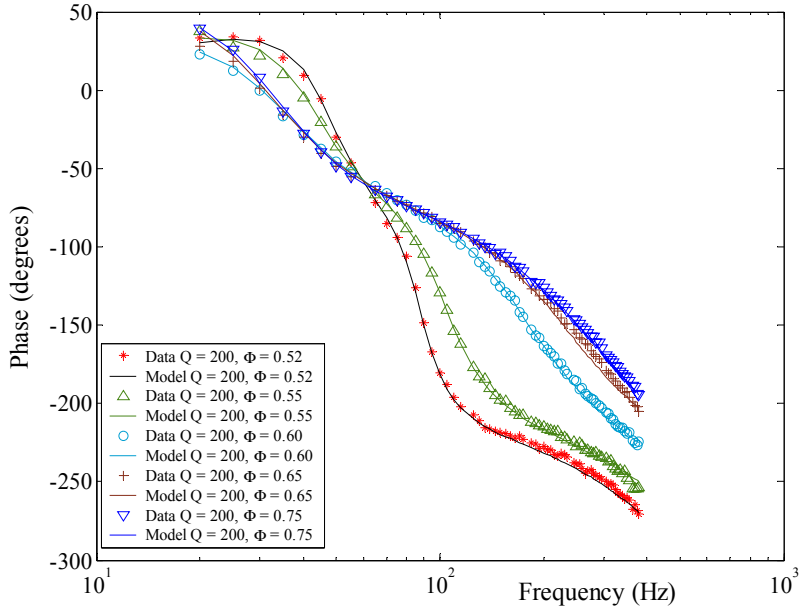

Figure 6.32: FRF (phase)for $Q_{Total} = 200$ cc/sec and propane-air mixture

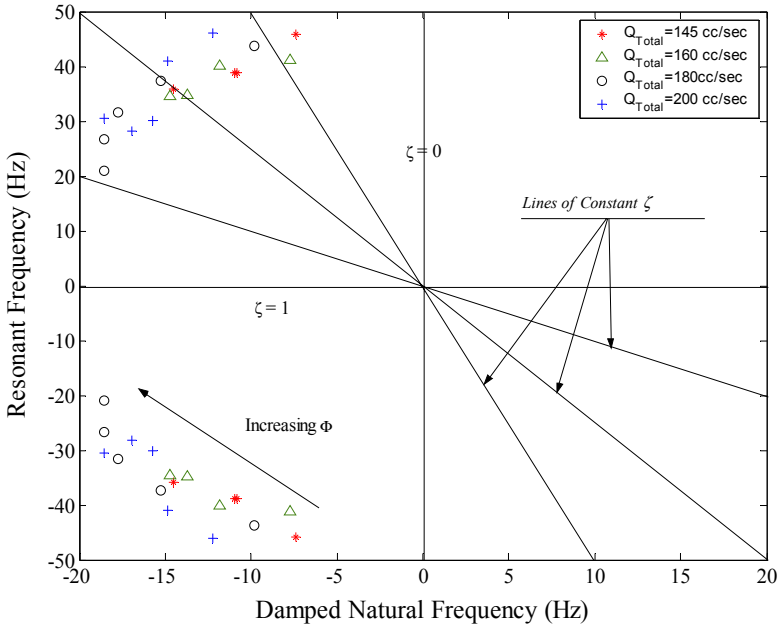

Figure 6.33: Phase plane for the 1^{st} resonant response, propane-air mixture

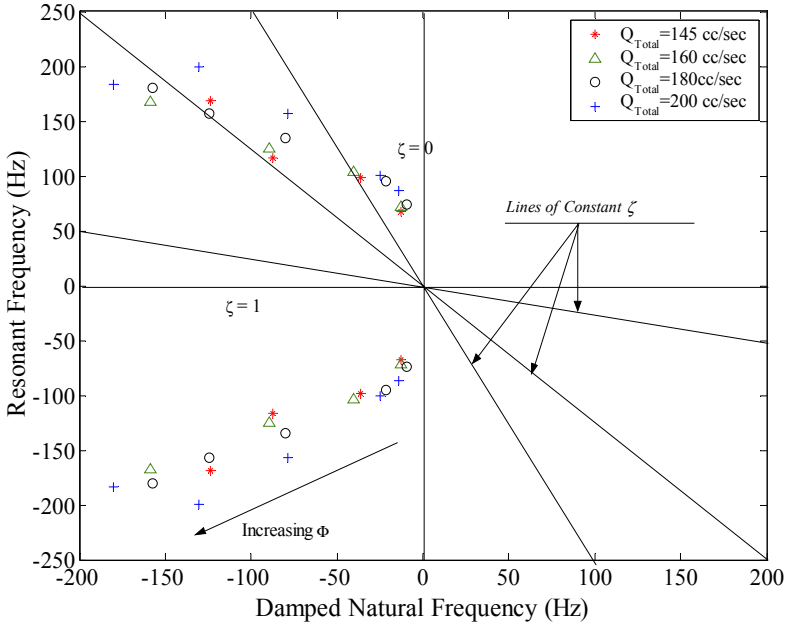

Figure 6.34: Phase plane for the 2^{nd} resonant response, propane-air mixture

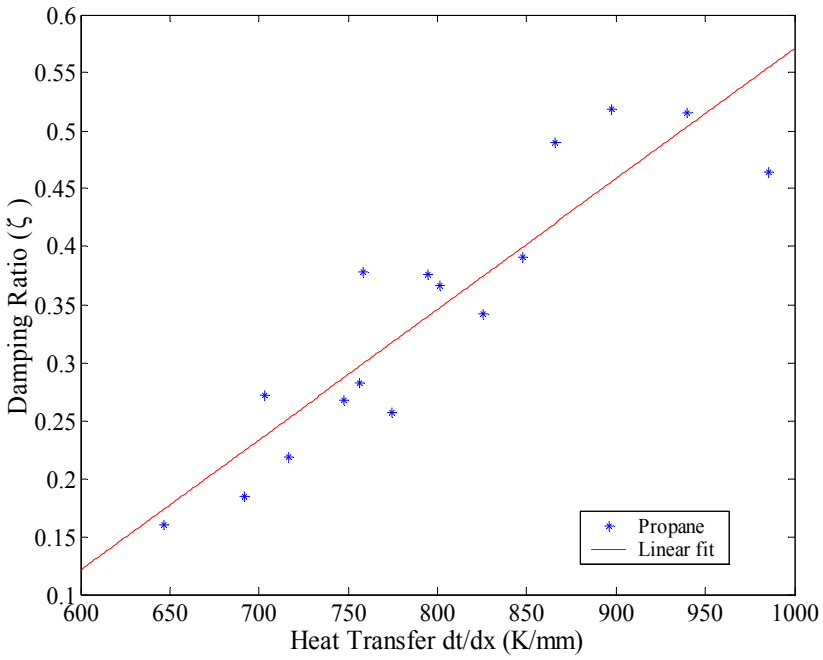

Figure 6.35: Dependence of ζ of the 1^{st} resonant response on the heat transfer potential

honeycomb and is shown in Figure 6.35. The estimation of $\frac{dT}{dx}$ was done by following the procedure described in Section 6.2.4, preserving the definition of all the parameters used. Figure 6.35 shows a linear dependence of the damping ratio to the heat transfer potential, thus once again confirming the conclusion that the first resonant response represents the fluctuations in the flame speed.

The frequency of the 2^{nd} resonant response varies between 67.5 Hz and 200 Hz. The damping ratio of the 2^{nd} resonant response exhibits two constant values. This behavior is consistent with that exhibited by methane-air flames. Therefore, the resonant frequency of the 2^{nd} resonant response was plotted against the flame temperature in Figure 6.36. The flame temperature used in Figure 6.36 was generated by modeling propane-air flames using 'Premix' and the detailed set of chemical reactions given by Dagaut et al. [78]. These set of reactions are also valid for ethane. The mechanism file was modified to incorporate OH^* mechanism proposed by Haber [70]. The resonant frequency behaves exponentially with temperature,

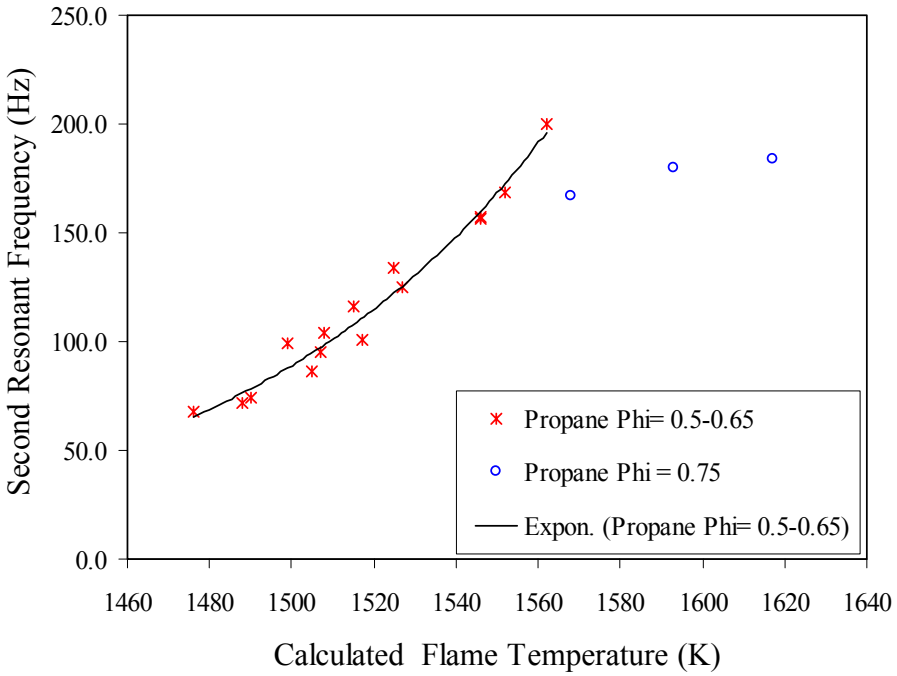

Figure 6.36: Frequencies of the 2^{nd} resonant response plotted as a function of flame temperature

thus re-confirming that the 2^{nd} resonant response represents the dynamics of the chemical kinetics. From Figure 6.34, it is seen that by lowering the equivalence ratio, the 2^{nd} resonant response moves closer to the resonant frequency axis. If the curve that fits these poles is extrapolated, it is expected to cross the resonant frequency axis at about 55 Hz. Thus, lowering Φ below 0.55 would eventually push the 2^{nd} resonant response into the right half of the 's plane' and render the system unstable. This was observed for $\Phi = 0.5$ and is plotted earlier in Figure 6.24.

Time delay was predicted using the 'Premix' calculations on the basis of the procedure described in Section 6.2.5. This predicted delay was compared with the time delay used in generating the reduced order model and is plotted in Figure 6.37. The deviation of the value used in generating reduced order models from the time delay predicted using 'Premix' is within 25 % for almost all cases, except for a couple of conditions at $Q_{Total} = 200$ cc/sec. This can be considered to be a reasonable match, considering the limitations of the comparison

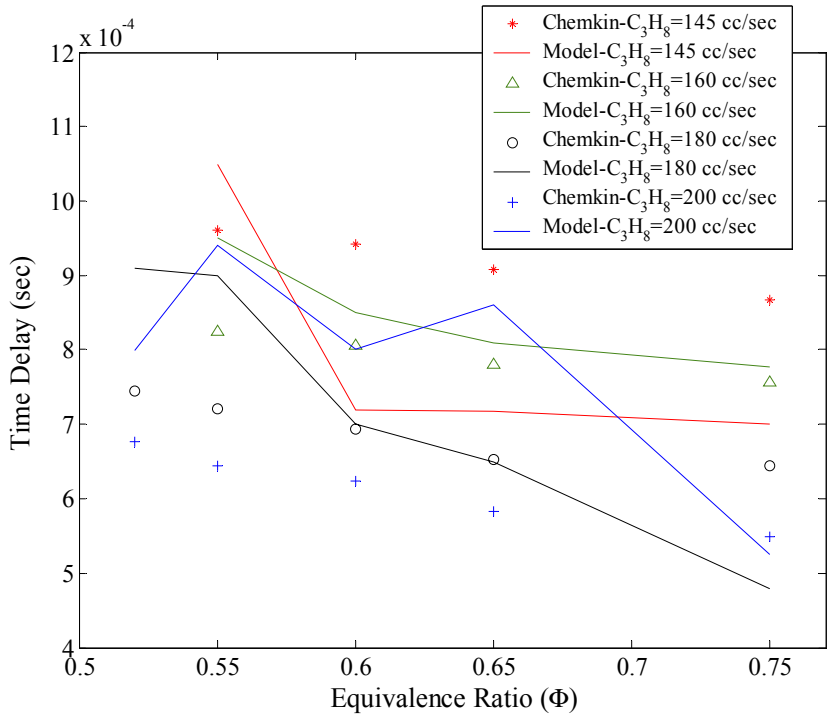

Figure 6.37: Time delay as a function of Φ for propane-air mixture

as described in Section 6.2.6.

6.3.2 Dynamics of Ethane-air Flames

Premixed mixture of instrument grade ethane and air were studied for four equivalence ratios ranging from 0.55 to 0.75 and four flow rates ranging from 145 cc/sec to 200 cc/sec. The parametric conditions studied were chosen so as to be able to compare the results with those of the methane-air and propane-air combustion experiments. However, below $\Phi = 0.55$ the flame could not be stabilized over the honeycomb, thus constraining the parametric range of the experiment. Additionally, for a $Q_{Total} = 145$ cc/sec and $\Phi = 0.55$, the flame was stabilized over the honeycomb but no experimental data could be obtained as the flame exhibited dynamic instabilities that rendered it impossible to generate accurate dynamic models based on linear systems theory.

Figure 6.38 through Figure 6.45 shows the magnitude and the phase of the FRF between

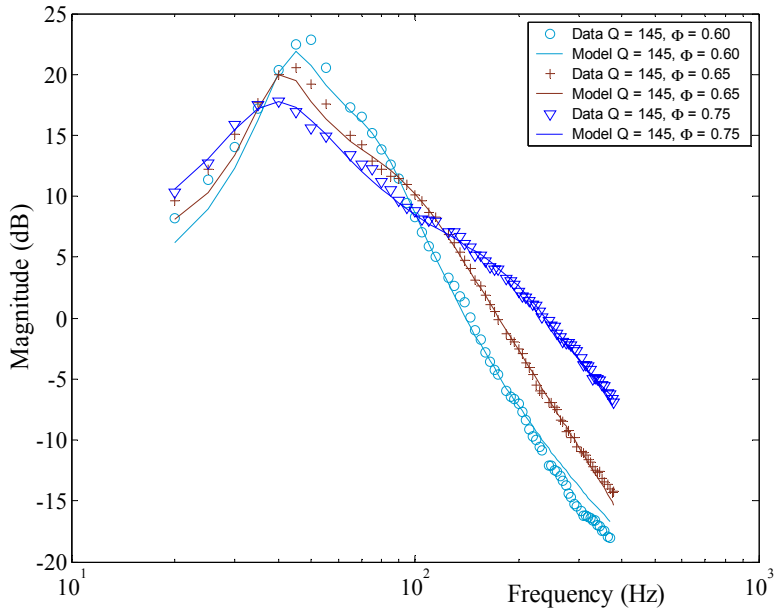

Figure 6.38: FRF (magnitude) for $Q_{Total} = 145$ cc/sec and ethane-air mixture

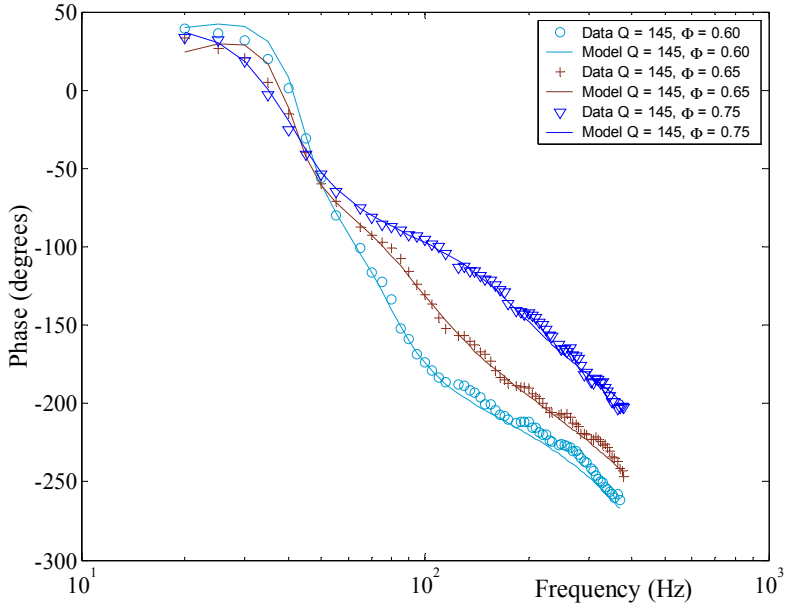

Figure 6.39: FRF (phase) for $Q_{Total} = 145$ cc/sec and ethane-air mixture

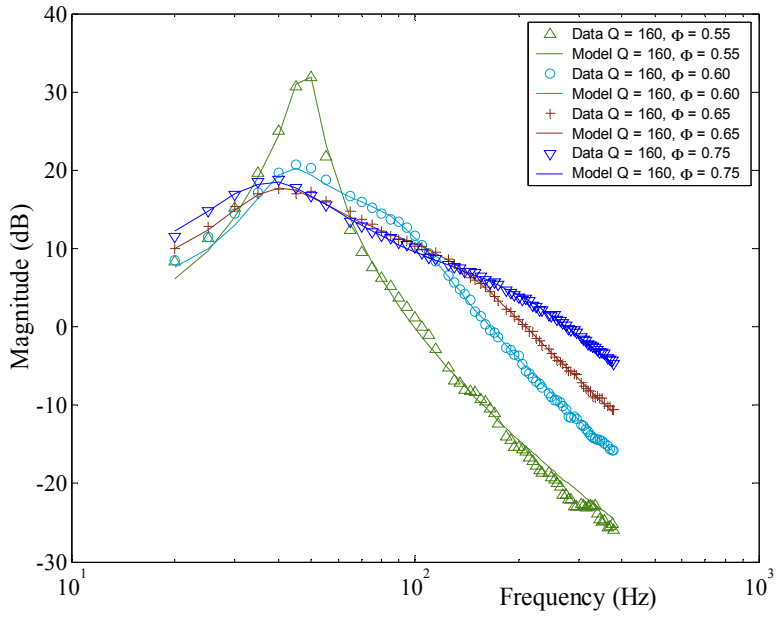

Figure 6.40: FRF (magnitude) for $Q_{Total} = 160$ cc/sec and ethane-air mixture

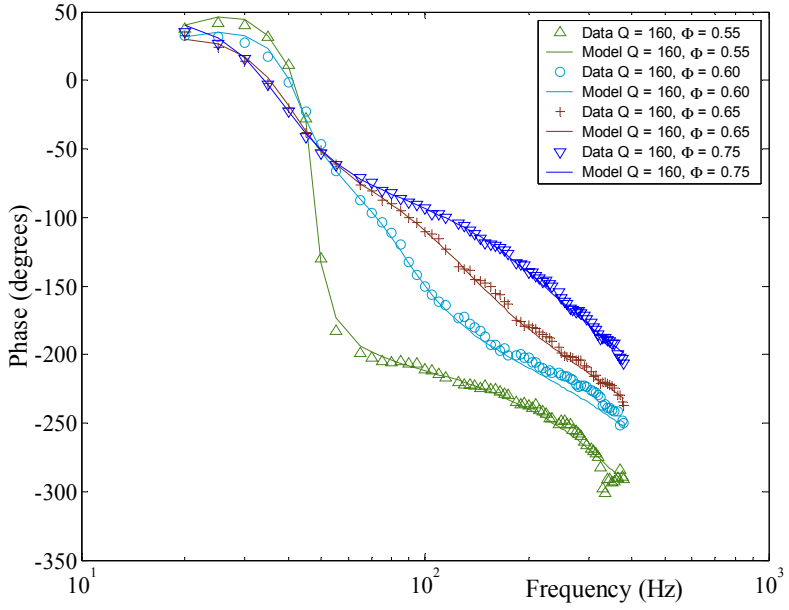

Figure 6.41: FRF (phase) for $Q_{Total} = 160$ cc/sec and ethane-air mixture

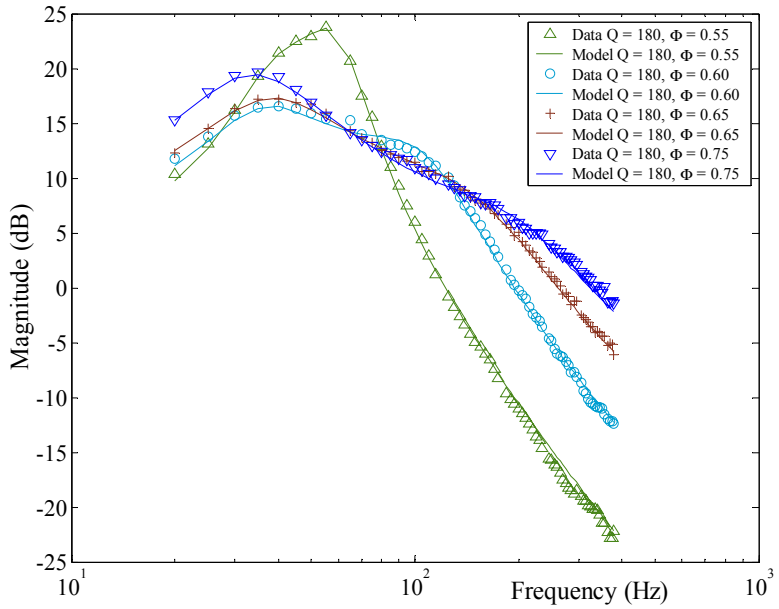

Figure 6.42: FRF (magnitude) for $Q_{Total} = 180$ cc/sec and ethane-air mixture

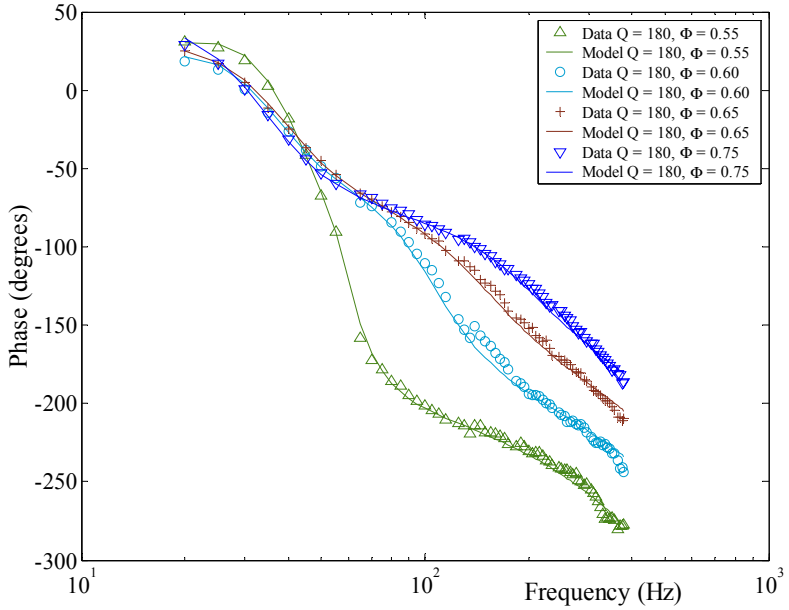

Figure 6.43: FRF (phase) for $Q_{Total} = 180$ cc/sec and ethane-air mixture

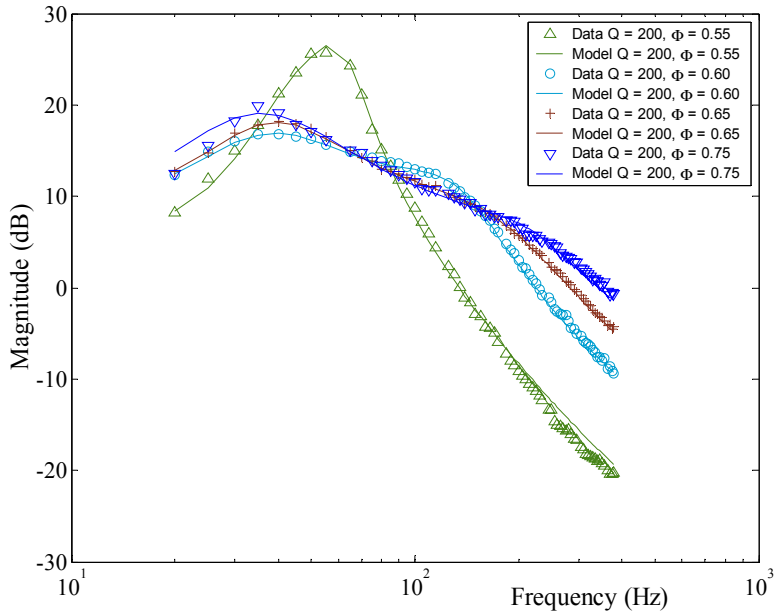

Figure 6.44: FRF (magnitude) for $Q_{Total} = 200$ cc/sec and ethane-air mixture

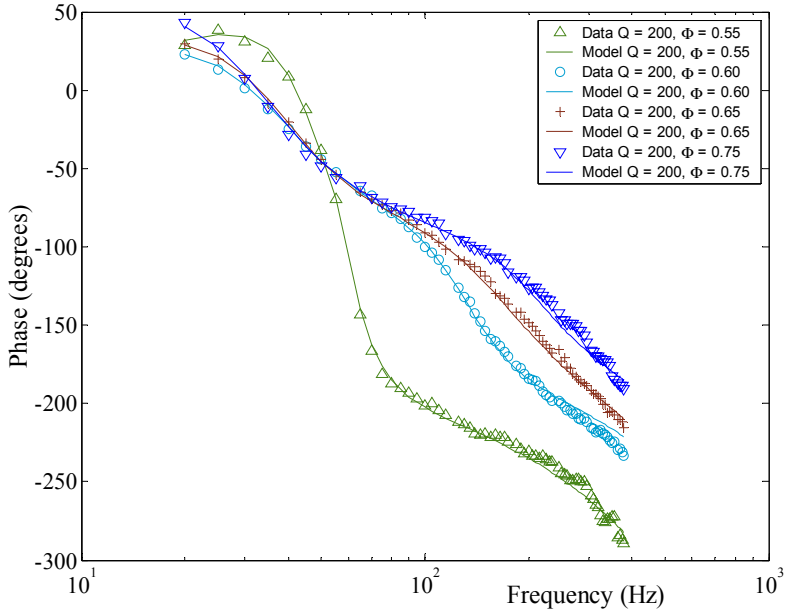

Figure 6.45: FRF (phase)for $Q_{Total} = 200$ cc/sec and ethane-air mixture

the OH^* chemiluminescence signal and the u' for the four flow rates of 145 cc/sec, 160 cc/sec, 180 cc/sec and 200 cc/sec. Both the magnitude and the phase plots of the FRF show similar characteristics, as noted for methane-air flames and propane-air flames described earlier in this chapter. The FRF exhibits characteristics of a fourth order system. The 1^{st} resonant response is in the frequency range of 30 to 45 Hz, and exhibits significant increase in damping with increase in Q_{Total} and Φ. The 2^{nd} resonant response is rather damped except for $\Phi = 0.55$, and increases in frequency with increase in Q_{Total} and Φ, and is primarily responsible for broadening of the bandwidth.

Empirical system models were generated for the full set of experimental data of ethane-air flames using the Controls Tool Box of Matlab and the procedure described in Section 6.2.3. The models that best represent the experimental data predict the dynamics to be of fourth order with a pure time delay, a behavior similar to that of methane-air and propane-air premixed flames. The model predictions are plotted over their respective data sets in Figure 6.38 through Figure 6.45. The models replicate the data reasonably well, except for the condition of $Q_{Total} = 145$ cc/sec and $\Phi = 0.55$, where the magnitude predicted by the model for the higher end of the frequency range is different from the experimental results by a couple of decibels. The model generated parameters; poles, zeros, gain and τ are tabulated in Appendix D.

The two resonant responses predicted by the model were plotted on the 's plane'. The 1^{st} resonant response is shown in Figure 6.46, while the 2^{nd} resonant response is shown in Figure 6.47. Similar to previous two fuels, the 1^{st} resonant response has its resonant frequency limited to the range of 30 to 45 Hz, while increase in the mean energy content of the mixture significantly increases its damping. Therefore, the damping ratios were plotted as a function of $\frac{dT}{dx}$ and is shown in Figure 6.48. $\frac{dT}{dx}$ was calculated as per the procedure described in Section 6.2.4. Figure 6.48 shows a linear dependence of the damping ratio on $\frac{dT}{dx}$, a characteristic feature also seen for methane-air flames and propane-air flames. This further supports the conclusion drawn that the 1^{st} resonant response represents the dynamics of flame speed oscillations.

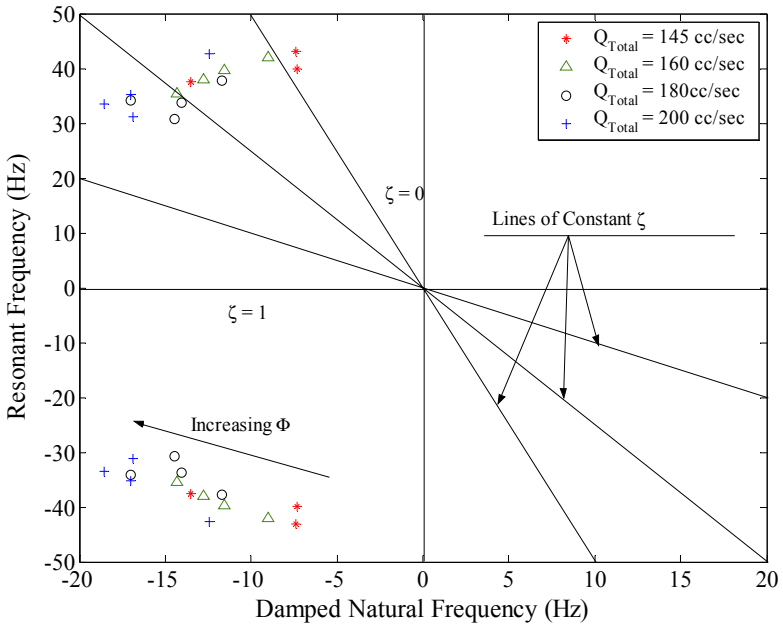

Figure 6.46: Phase plane for the 1^{st} resonant response, ethane-air mixture

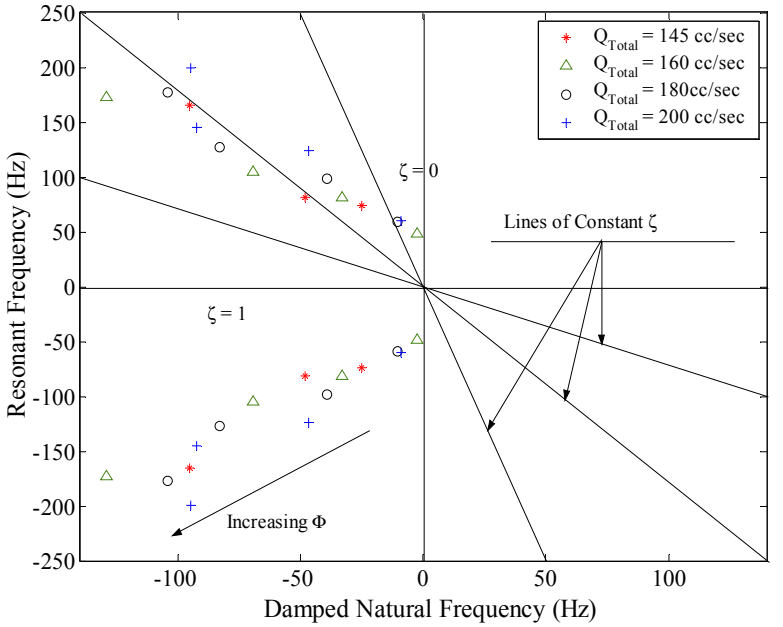

Figure 6.47: Phase plane for the 2^{nd} resonant response, ethane-air mixture

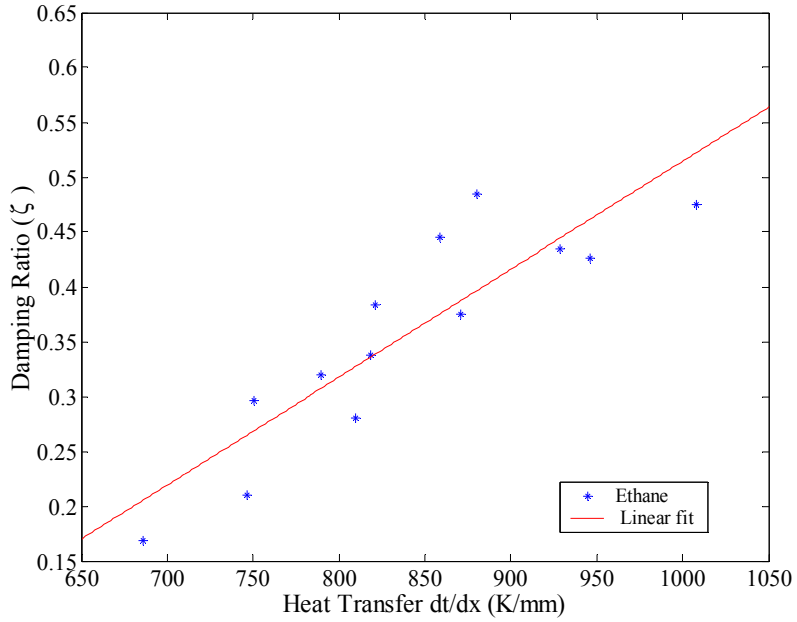

Figure 6.48: Dependence of ζ of the 1^{st} resonant response on the heat transfer potential

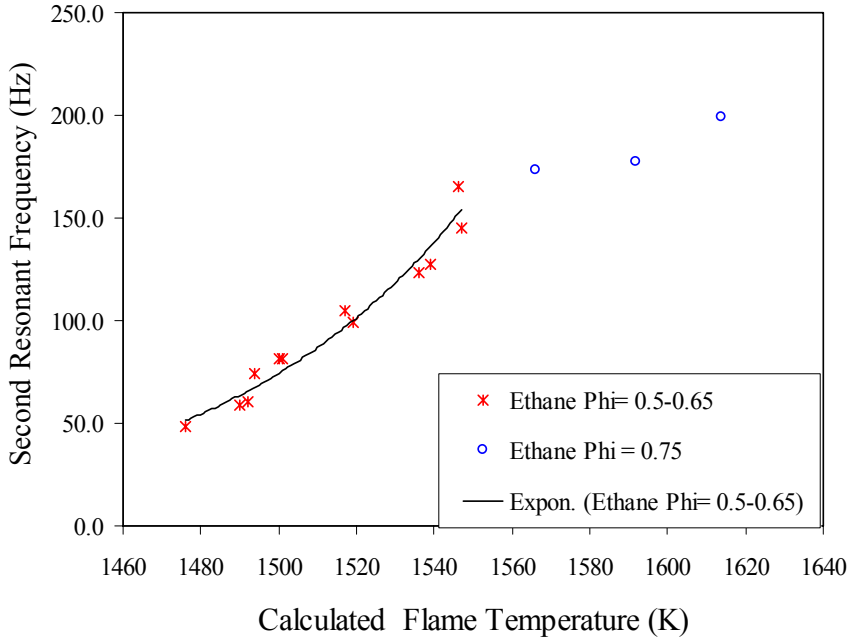

Figure 6.49: Frequencies of the 2^{nd} resonant response plotted as a function of flame temperature

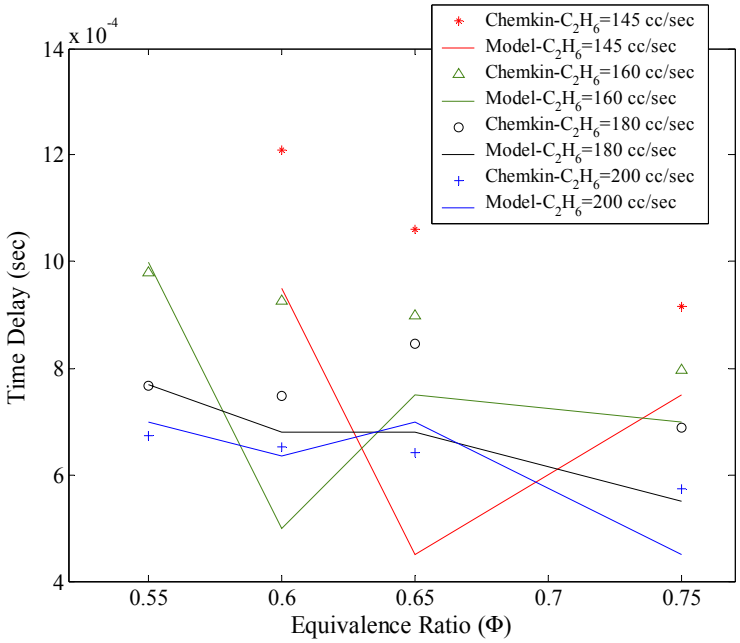

Figure 6.50: Time delay as a function of Φ for ethane-air mixture

The 2^{nd} resonant response has its resonant frequency varying between 48 Hz and 200 Hz, and it exhibits a constant damping for the data sets that were recorded for $\Phi \geq 0.6$. The data sets recorded for $\Phi = 0.55$, together exhibit another damping ratio. The behavior of the 2^{nd} resonant response for ethane-air flames is very similar to that of methane-air and propane-air flames. The resonant frequency of the 2^{nd} resonant response shows an exponential dependence on the modeled flame temperature, as is graphically shown in Figure 6.49. Thus, the conclusion that the 2^{nd} resonant response represents the dynamics of the chemical kinetics is further strengthened.

The time delay used in the development of the reduced order model was compared to the time delay calculated from the 'Premix' code and is plotted in Figure 6.50. The discrepancy between the two values is within 25% for most cases except for the condition of $\Phi = 0.65$, $Q_{Total} = 145$ cc/sec and the condition of $\Phi = 0.6$, $Q_{Total} = 160$ cc/sec, where the deviation in the modeled time delay and τ_{chem} is about 50 %. Considering the limitations of this comparison as described in Section 6.2.6, the results shown in Figure 6.50 can be considered to be a reasonable match.